Complex patterning in jerky flow from time series analysis and numerical simulation

Claude Fressengeas, Tatiana Lebedkina, Mikhail Lebyodkin

Complex patterning in jerky flow from time series analysis and numerical simulation

Claude Fressengeas, Tatiana A. Lebedkina and Mikhail A. Lebyodkin
Laboratoire d'Etude des Microstructures et de Mécanique des Matériaux
Université de Lorraine/CNRS/Arts et Métiers ParisTech
7 rue Félix Savart, 57070 Metz, France
claude.fressengeas@univ-lorraine.fr

January 11, 2024

Abstract

The paper is a tribute to Ladislas P. Kubin's long-standing work on the collective behavior of dislocations in jerky flow. In a first part, it reviews his contributions to the statistical, dynamical and multifractal analyses carried out on stress-time series recorded from both single crystals and polycrystalline samples of dilute alloys subjected to tensile tests at constant strain rate. Various spatio-temporal dynamical regimes were found as the applied strain rate was varied. Type C static bands were associated with quasi-random collective behavior, the hopping type B and propagating type A bands could be shown to correspond to chaotic and self-organized critical dynamics, respectively. The crossover between the A and B regimes was characterized by a large spread in the multifractal spectrum of stress drops, associated with heterogeneity of the dynamics. In a second part, the paper reviews the nonlocal models Ladislas inspired to interpret these results from numerical solutions of the boundary value problem, on the basis of dynamic strain aging, the incompatibility stresses associated with dislocations, their plastic relaxation and the spatial couplings they inherently involve. Eventual developments of this research, rooted in the same ideas, on the statistical and multifractal analyses of the accompanying acoustic emission are reviewed and discussed in terms of the synchronization of small-scale plastic events.

1 Introduction

Jerky flow or the repeated yielding of dilute alloys has been studied since the turn of the nineteenth century [1, 2], and it continues to retain the attention of the materials research community, well into the twenty first century [3, 4]. Observed in many alloys [5, 6], it is one of the most striking examples of the complexity that can emerge from the spatio-temporal dynamics of large dislocation ensembles. In a tension test with a constant applied strain rate, the Portevin–Le Chatelier effect (PLC), as it is also referred to, manifests itself as a series of serrations in the stress-time or strain curve. Each stress drop is associated with the nucleation of a band of localized plastic strain, which, depending on the experimental conditions, may or may not propagate along the sample. The continued interest in the PLC effect arises not only from the wealth of spatio-temporal patterns it generates, but also from the need to ease its detrimental influence on the mechanical properties of the material. Indeed, it affects the ductility and appearance of sheet metal, and impacts usage of aluminum autobody sheet [7, 8, 9]. Plastic flow localization into bands results in non uniform thinning and affects the formability and visual aspect of the material; fracture properties are also influenced by strain aging, although it is not clear as yet if they are improved or diminished [10, 11, 12, 13].

It is now widely accepted that the microscopic origin of the PLC effect is the Dynamic Strain Aging (DSA) of solute alloys arising from the interaction between mobile dislocations and diffusing solute atoms [5, 14, 15, 16, 17] . In a certain range of strain rates and temperatures, the

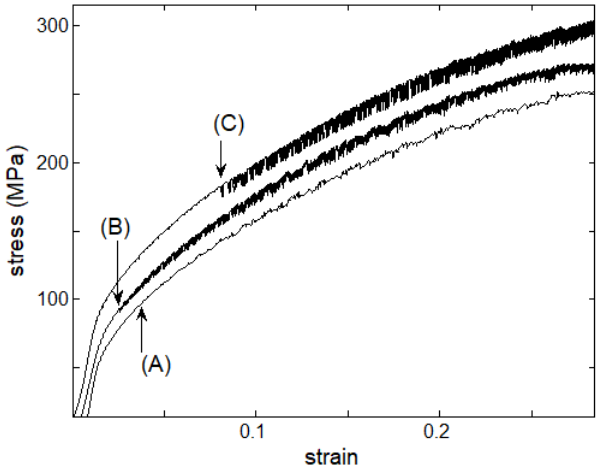

Figure 1: A, B, C serration types in a $Al-3\%Mg$ polycrystal, loaded at room temperature and strain rates (A) $6\times10^{-3}s^{-1}$, (B) $2\times10^{-4}s^{-1}$, (C) $2\times10^{-5}s^{-1}$. On each curve, the arrow indicates the critical strain ϵ_{cr} for the onset of the PLC effect. Note the decreasing amplitude of the serrations as the strain rate increases. After [18], with permission of the Editor.

waiting time of the dislocations temporarily arrested at obstacles becomes of the order of the diffusion time of the solute atoms. In such conditions, these atoms can diffuse to and age to some amount the arrested dislocations before they break away from their obstacles. As a result, the stress needed to unpin the dislocations increases with increasing waiting time and decreasing strain rate, in sheer contrast with standard thermally activated phenomena. At the macroscopic scale, this inverse force vs. flux relation translates into a range of negative sensitivity of the flow stress to the strain rate. When the imposed strain rate falls into this range, the uniform plastic deformation of the sample becomes unstable. Bands of localized plastic deformation nucleate, and serrations appear in the stress-time or stress-strain series. On increasing the strain rate in this range (or decreasing the temperature), one observes serrations of decreasing amplitude, with an increasing tendency to band propagation. In polycrystals, the usual metallurgical taxonomy separates three generic types of serrations, namely types A, B and C, mainly on the basis of their visual appearance (see Fig.1) [19, 20, 21]. Type C serrations, with large characteristic stress drops, associated with static bands more or less randomly located along the sample, are observed at the lowest strain rates in the range of negative Strain Rate Sensitivity (SRS) of the flow stress. Type B serrations with smaller stress drop amplitudes are found at medium strain rates. The bands are still static in nature, but a new band consistently nucleates ahead of the previous one, giving the visual impression of a hopping propagation. Finally at the highest strain rates in this range, one observes type A serrations with still smaller stress drops, associated with continuously propagating bands. Being essentially qualitative, this typology must be understood as a mere visual guide. The stress drops may display various peculiarities in the complex solute alloys often used in industrial samples, which makes the serrations hardly reducible to the generic types A, B and C, and calls for a more quantitative basis for classification.

This wealth of spatio-temporal features has long defied full understanding. Under the insightful and inspiring guidance of Ladislas P. Kubin and with the help of his comprehensive knowledge of dislocation properties, renewed perspectives emerged in our group both from connections made with nonlinear dynamics in data analysis and from nonlocal formulations in modeling approaches [22]. The present paper is a tribute to Ladislas' work and an acknowledgment of the role he has been playing in this group for about 20 years, and more generally in the material research community dedicated to jerky flow studies, that of a friendly mentor with deep insights into DSA, dislocation dynamics and plastic instability, as well as crisp and

perspicuous views on the scale transitions and modeling achievements needed at all scales of resolution to account for the fundamental aspects of jerky flow. The paper intends to revisit in a synthetic way both the analysis of spatio-temporal dynamics of jerky flow in single and polycrystals he inspired, and the modeling approaches he contributed to develop for their interpretation. It further reviews eventual developments of this approach, rooted in the same basic ideas to the analysis of the time series of the accompanying Acoustic Emission (AE). However, it is not meant to cover extensively the current state-of-the-art, neither in modeling approaches nor in experimental studies or in data analysis. It may suffice to note that the ideas developed by Ladislas P. Kubin for conventional solute alloys have been permeating numerous studies devoted to the self-organization of intermittent plastic deformation processes in various novel materials, such as high/medium entropy alloys or bulk metallic glasses [23, 24, 25, 26, 27, 28].

As just mentioned above, connections were made in our group with the methods used in nonlinear dynamics to analyze complex oscillatory time series. The undertaken approach boils down to answering a couple of simple questions: are the seemingly disordered stress vs. time series recorded during jerky flow purely random, or are they underpinned by some hidden order, from which some physical consequences could be drawn? More precisely, is there any correlation between the various spatio-temporal manifestations of the phenomenon, *i.e.* the different types of localized deformation bands and stress vs. time serrations, and some possibly different underpinning dynamical regimes when the applied strain rate (or the temperature) is varied? Further, are these prospective correlations dependent on the scale of the observation, namely when shifting from stress time-series to the time series of the accompanying AE? Finally, what would be the physical consequences of any such dependence?

At first, a rather straightforward answer to some of these questions was provided by statistical analyses of the stress drops, which showed that the distributions of stress drop magnitudes and durations shifted from bell-shaped at low and medium strain rates to power-laws at high strain rates in model binary alloys. In the former case, the statistics clearly suggest the existence of characteristic average stress drop durations and magnitudes at low and medium strain rates, whereas they imply that such intrinsic stress and time scales are lacking at high strain rates. A more difficult but also more revealing way of dealing with the stress vs. time series consists in analyzing the dynamical regime using the powerful data processing techniques developed in the field of nonlinear dynamics. Prospectively, the dynamics may either be randomness, or an underlying order may exist, such as deterministic chaos characterized by only a few degrees of freedom [29], for which a prediction had been made [30], synchronization of plastic events [31], or Self-Organized Criticality (SOC) [32, 33], which involves infinite degrees of freedom, in sheer contrast with chaos. Amazingly, although they are very different in nature, all the above-mentioned dynamic regimes were found in the range of existence of the PLC effect in both single and polycrystals. Hence, owing to this diversity and to the vagueness of the standard typology of stress drops, we looked for some common methodology leading to their quantitative characterization. Such a common measure was provided by their multifractal analysis [34].

From the modeling point of view, the basic question was therefore: what are the minimal features to be introduced into models to retrieve both this wealth of temporal dynamics and the various localized strain band patterns conventionally observed in single and polycrystals when strain rate is varied? It was anyway taken for granted that the Kubin-Estrin "local" model for DSA [35, 36] or its version coupling dislocation and solute dynamics [37] had to be adjoined to visco-plasticity in a finite element discretization of the $3D$ boundary value problem, and that some kind of "non locality" had to be present to account for band propagation and spatial coupling [22, 38, 39]. Spatial correlations are often taken to have two main origins in plasticity: the long-range stresses arising from the elastic interactions between dislocations and the short-range interactions deriving from their transport through the material. However, it should be borne in mind that it also derives in the first place from the continuity of matter and mechanical

equilibrium. Hence, the above question actually translates into the following one: what are the minimal non local features to be introduced into models to retrieve the complex spatio-temporal dynamics observed in both single and polycrystals when strain rate is varied in the presence of DSA [40, 41]? Besides, if such models can be found, what kind of dynamics do they predict in the absence of DSA, for the remaining small scale plastic events [42]?

The paper is therefore organized as follows. Overall experimental issues encountered in mechanical testing and data recording methods are outlined in Section 2. Section 3 reviews the different dynamical and multifractal methodologies used for analyzing the recorded time series. The results for single and polycrystals are summed up in Section 4. Section 5 recalls the essential features of the modeling approaches, including their treatment of DSA and the spatial correlations they involve, as well as the main results of the simulations. An overall discussion of the experimental and theoretical results of Sections (4,5) is provided in Section 6. Conclusions follow.

2 Experimental

Rather than providing extensive data on the compositions and machining processes of the materials used in the experimental studies referred to in this paper, for which the reader is referred to the original publications, this section is focused on the general issues that need to be faced in jerky flow studies, where it is attempted to characterize complex time evolutions involving large numbers of individual plastic events occurring at different spatial locations, in unsteady systems evolving far from stable equilibrium with various characteristic time scales. Monitoring such evolutions commonly requires both spatially averaged signals, such as stress or Acoustic Emission (AE) time series, and local records as provided by high speed Digital Imaging Correlation (DIC) techniques. In monitoring average signals, the challenge is to extract information from overall data recorded at the scale of the sample on the spatio-temporal correlations that are at the root of patterning at micro-scale level. Put differently, it is to extract information on the collective behavior of dislocation slip events occurring during plastic instabilities, from the investigation of their impact on physical properties observed at meso-scale in AE time series, or at macro-scale in stress time series or DIC records. The DIC techniques and similar methods have indeed been applied to both smooth and jerky flow to assess the meso-scale complexity of the material's response [42, 43, 44], but this aspect of the investigations will not be treated in the present paper.

In recording the stress time series, choosing the strain range to be sampled along the stress vs. strain curves and the sampling frequency calls for great care. The sampling frequency must, on the one hand, be large enough to provide at least a few data points during the fastest events, viz. the stress serrations, but on the other hand, be small enough to avoid unnecessarily large data sets. The latter limitation may seem obsolete at present, due to the high storage capacity of modern recording systems. However, this seemingly "old-fashioned" precaution remains meaningful. Indeed, if coarsening the time resolution may result in a loss of high-frequency information, reducing it may lead to missing the forest for the trees, *i.e.* hiding useful information behind noise that is otherwise automatically smoothed out at a lower resolution. Noise may become embarrassing regarding the sample response when it corresponds to a frequency range similar to that of the fast deformation events. As a matter of fact, noise reduction has been (and still is) a challenge in studying collective dislocation dynamics, as will be seen below in Section 3.1.2.

The experimental stress vs. strain curves often display transient strain hardening, associated with a drift of the dislocation micro-structure on a slow time scale, much larger than the fast characteristic time scales of the serrations, *i.e.* the stress drop duration and the reloading time between some given drop and the next one. Such a micro-structural drift is, to a large degree, foreign to the repetitive instability problem under investigation. Furthermore, an increase in

the average size of the stress drops is systematically observed with increasing strain, a rather common feature of jerky flow, also due to strain hardening. In order to alleviate the impact of such a slow time scale evolution on the study of fast time scale events, the statistics have most often been be sampled on data sets free of any such significant drift, in practice for strains large enough to lead to saturation of strain hardening. Besides, the average stress drop size may need to be normalized and leveled off, for example by using a moving average procedure. In fact, the normalization procedure may sometimes be sufficiently efficient to allow handling data corresponding to a significant work hardening, *e.g.*, during the initial stages of deformation [45]. All the investigations presented in this paper were carried out on time series resulting from such preliminary treatments.

The AE technique has been one of the most popular methods applied to a high-frequency characterization of plastic deformation since about a century [46]. Various quantitative approaches have been developed to extract information from an acoustic signal at various levels of time resolution (see *e.g.* [47]). The present paper mainly illustrates a statistical and multifractal analysis designed in the same spirit as that applied to the stress-time series. At least, one obvious advantage of this choice is that it allows for a direct comparison of the conclusions on collective dislocation dynamics that arise at different resolution length scales from two physically different aspects of the material's response to straining.

The main approach to data collection is based on the real-time detection of acoustic events, or hits, accompanying plastic flow, by virtue of a software built-in any acoustic system. The starting point of an event is clearly defined as the instant when the amplitude of sound oscillations exceeds a preset threshold, usually selected at the noise level in the idle state. The main intricacies concern the definition of the event's ending point, due to secondary echoes caused by multiple sound reflections within the deforming sample. The usual criterion uses the so-called Hit Definition Time (HDT): the event is considered to terminate at the instant after which the sound oscillations amplitude remains under the threshold at least during the HDT. The difficulty met on this way is that the echo return time is very short for metallic samples with a typical gauge length of several centimeters. The estimate of this time does not exceed about $10\,\mu s$ even for the longest path, *i.e.* the double sample length when the reflected signal comes from its opposite end. The common way to proceed in the case of metals is to choose a relatively high HDT to include all secondary echoes into the main hit. By varying the HDT up to $600\,\mu s$, it was shown that the AE amplitude statistics were very robust, provided HDT $\geq 40\,\mu s$ [48]. This rule was respected in all the statistical studies reported in the paper.

The inclusion of secondary echoes, as well as the concomitant difficulty to isolate closely following hits corresponding to different AE sources, inevitably alter the measurement of the hit duration [49]. Besides complicating the interpretation of the recorded durations, this uncertainty also affects the choice of the appropriate AE characteristics for a statistical analysis. One of the common approaches in the literature is to assess the statistics of the hit energy evaluated as the time integral of the squared value of the signal amplitude, $A^2(t)$, over its duration [50]. Checking this statistics at mesoscopic scale is consistent with the statistical analysis of the stress serration size, $\Delta\sigma$, at macroscopic scale. Indeed, as the stress drop is determined by the elastic unloading of the sample-machine system to the strain jump caused by an abrupt plastic event, $\Delta\sigma$ is proportional to $\Delta\epsilon$, and it provides a proxy for the dissipated mechanical energy, $\sigma\Delta\epsilon$ (σ is considered as approximately constant since $\Delta\sigma \ll \sigma$). However, the hit duration being an ill-defined parameter, we instead followed [51], and the squared peak amplitude, A^2, was used as an energy characteristic in our studies.

Some more remarks are noteworthy. The AE intensity evolves in the course of deformation. Its variations are material-dependent and not correlated in a unique way with work hardening. Consequently, the analysis was applied within time intervals where the average AE intensity was

approximately constant, and the robustness of the results was checked by using several bounds for the selected time intervals. In addition, the probability densities were calculated with data normalized by the average values over the statistical sample, be it for $\Delta\sigma$ or A^2, at the macroscopic or mesoscopic scales. Besides collapsing all data onto a unified scale range, this approach allowed to avoid arbitrariness in the choice of the bin size.

Finally, besides the statistical and multifractal analysis of series of AE events, the paper will present some of the first examples of the multifractal analysis of the "raw", *i.e.* continuously measured AE signal, in order to unveil the correlations in the dislocation dynamics on finer time scales pertaining to the deformation processes at work during individual stress serrations.

3 Methodology

3.1 Stochastic vs. chaotic time series

3.1.1 Randomness vs. chaos

As pointed out above, noise is an undesirable component of experimental data, to which it adds an unsuitable whiff of indeterminacy. It may not be part of the phenomenon of interest, as it may arise from the measuring instruments and the limitations to their accuracy, or from the experimental environment through its electrical, mechanical and thermal effects. It may also derive from a lack of knowledge of the phenomena contributing to the evolution in time of the system under scrutiny. A classical example is the Brownian motion of a particle, whose randomness arises from its innumerable contacts with the other particles of the reservoir. A deterministic prediction of the trajectory of the particle seems therefore impossible. However, it has now been comprehensively proven that the apparent randomness of an oscillatory time series may also result from the deterministic evolution of a system involving a few independent variables (at least three), commonly referred to as "chaotic" in the scientific literature [29], although the word "chaos" has long been (and still is) also casually used in common parlance as a synonym for pure randomness. Deterministic chaos, or simply chaos, manifests itself in the phase space of the system by the existence of a compact, self-similar attractor dubbed "strange attractor" for its involved appearance (see in Fig.2 the exemple of a PLC "strange" attractor). The existence of a strange attractor stems from its two fundamental stability properties, namely its linear local instability, which is counterbalanced by its nonlinear global stability. Linear instability implies "sensitivity to initial conditions": two points in the phase space initially separated by a small distance, however small, can be located far away from each other after a sufficiently long period of time, suggesting a "loss of memory of the initial state" similar to stochastic behavior. However, due to nonlinear global stability, both points end up being still located on the attractor, because their trajectories fold and eventually remain bounded in the phase space, in sheer contrast with stochastic trajectories filling the entire phase space, or with the infinitely diverging trajectories of catastrophic nonlinear instabilities. Boundedness and self-similarity of the resulting attractor are consequences of the combined diverging (associated with its linear instability) and folding (due to its nonlinear stability) properties of the trajectories.

3.1.2 Reconstructed phase space

Of course, the attractor and phase space of the system are unknown when the oscillatory time series, say: $\sigma(i), i \in (1, 2, \ldots, N)$, where i is in units of the sampling time interval Δt and N is the number of data points, derives from an experimental data set. However, the attractor can be reconstructed by unfolding the one-dimensional time series into a d-dimensional embedding space through the introducion of the $(N - (d-1)\tau)$ vectors

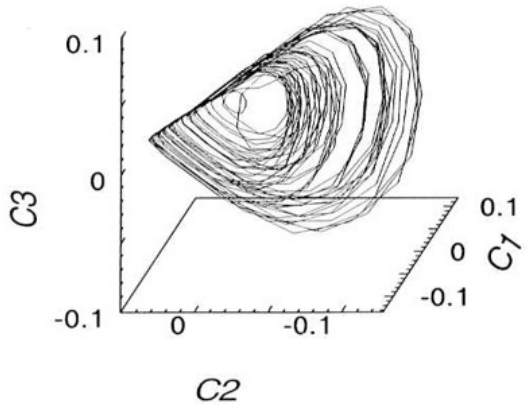

Figure 2: Projection in the reconstructed phase space of a chaotic attractor onto the $3D$ subspace spanned by the three eigenvectors of the trajectory matrix corresponding to its three largest principal values. $Al-2.8\%Mg$ polycrystal loaded at $\dot{\epsilon}_a = 6.67 \times 10^{-5} s^{-1}$. After [52], with permission of the Editor.

$$\mathbf{X}_i = [\sigma(i), \sigma(i+\tau), ..., \sigma(i+(d-1)\tau)]\,; i = 1, ..., N-(d-1)\tau \tag{1}$$

where τ defines a delay time. The vectors $\mathbf{X}_i$ define $(N-(d-1)\tau)$ points along an orbit or a trajectory called the "reconstructed attractor" in the d-dimensional embedding space, itself referred to as the "reconstructed phase space", and it is expected that the properties of the reconstructed attractor mimick those of the actual attractor in the actual phase space [53]. A key issue in this reconstruction process is the choice of the delay time τ and reconstruction dimension d for a proper rendition of the actual dynamics [22]. The correlations will be underestimated if the delay time is too long as compared with the characteristic time scale of the phenomenon (here the stress drops), due to the exponential divergence of nearby orbits, or overestimated if it is too short, as if the measurements were made nearly at the same time. As a rule of thumb, the delay time may be taken of the order of the time at which the autocorrelation function falls to $1/e$ of its initial value [54, 55]. Similarly, two points may appear as neighbors on the attractor if the embedding dimension d is too small, which artificially increases the correlations, but cease to be neighbors when the embedding dimension is increased beyond the dimension of the actual phase space. Thus, increasing d lowers the contribution of false neighbors to such quantitative characteristics of the attractor as its Lyapunov exponents and correlation dimension, both to be reviewed below. Hence, a proper equivalence is obtained if the embedding dimension is large enough, but too large embedding dimensions do not bring the correct insights about the number of independent variables, while needlessly increasing computation costs. Further, the time series should be long enough, and noise should be reduced as much as possible. A convenient way to reduce noise is based on the Singular Value Decomposition of the $(d \times N)$ trajectory matrix $\mathbf{A}$:

$${}^t\mathbf{A} = \frac{1}{\sqrt{N}}[\mathbf{X}_1, \mathbf{X}_2, ..., \mathbf{X}_N] \tag{2}$$

In this method, the matrix $\mathbf{A}$ is rotated onto the basis of its principal vectors. The d principal values of matrix $\mathbf{A}$ (*i.e.* the eigenvalues of the $(d \times d)$ covariance matrix ${}^t\mathbf{A}.\mathbf{A}$) are positive; conventionally they are ordered in a decreasing order. If some principal values, say $(q+1, ..., d)$, are zero, or at least much smaller than the first q ones, then the trajectory remains essentially confined to the subspace spanned by the first q principal vectors. Thus q gives an estimate of the minimum dimension required for a proper dynamical description of jerky flow, while the $(d-q)$ last components may be dropped off as supposedly representing the contribution of noise to the time series. This distinction of some eigenvalues being much larger than the others allows

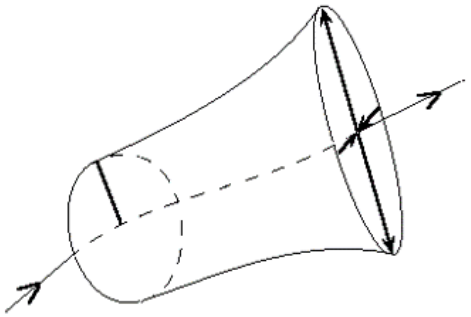

Figure 3: Sketch of stretching, contracting and neutral directions in the reconstructed phase space, with positive, negative and zero Lyapunov exponent, respectively. After [22], with permission of the Editor.

reducing the noise level in the calculation of the Lyapunov spectrum and correlation dimension, by using in the algorithms the matrix $\mathbf{A}$ truncated to its first q meaningful components and back-rotated to its canonical basis, instead of the original trajectory matrix $\mathbf{A}$ [56].

3.1.3 Sensitivity to initial conditions and Lyapunov exponents

The Lyapunov exponents are quantitative measures of the sensitivity to initial conditions. They reflect the rate of local divergence or convergence of neighboring trajectories in the phase space, as sketched in Fig.3. As this rate can be different for different orientations of the initial difference vectors, there are as many Lyapunov exponents as dimensions in the phase space. Most algorithms designed to retrieve their complete spectrum from the reconstructed phase space require very long time series, which are usually impractical to obtain. In the present work, we used a modified Eckmann algorithm suited for (not too) short time series [55, 57]. The algorithm relies on the construction of tangent $(d \times d)$ matrices $\mathbf{T}_i$ describing how time evolution sends small initial difference vectors around $\mathbf{X}_i$ to small difference vectors around $\mathbf{X}_{i+m}$:

$$\mathbf{X}_{j+m} - \mathbf{X}_{i+m} = \mathbf{T}_i.(\mathbf{X}_j - \mathbf{X}_i) \tag{3}$$

with $m \geq 1$. In a second step, the algorithm successively determines the orthogonal matrices $\mathbf{Q}_i$ and upper triangular matrices $\mathbf{R}_i$ such that $\mathbf{T}_i = \mathbf{Q}_i.\mathbf{R}_i$. The Lyapunov exponents λ_k are then given by

$$\lambda_k = \frac{1}{m\Delta t M} \sum_{j=0}^{M-1} \mathbf{R}_{j,ll}; k = 1, 2, ..., d \tag{4}$$

where M is the available number of matrices. Constancy of the λ_ks is checked over close neighbors $\mathbf{X}_j$ of $\mathbf{X}_i$ in a sufficiently large shell, as detailed in [52, 55]. A Lyapunov exponent is positive (negative) in a stretching (contracting) direction, null in the tangential direction of the orbit. Hence, chaos needs at least one positive Lyapunov exponent, whereas there is no positive exponent for stochastic systems. In addition, the analysis implies that chaos in a dissipative system needs at least three phase space variables, namely one for the stretching direction, one in the neutral direction along the orbit, and one for a contracting (dissipating) direction to ensure that their sum is negative (See Fig.4). The knowledge of all Lyapunov exponents allows computing the Lyapunov dimension D_{KY} from the Kaplan–Yorke conjecture [58]

$$D_{KY} = j + \frac{\sum_{i=1}^{j} \lambda_i}{|\lambda_{j+1}|}, \sum_{i=1}^{j} \lambda_i > 0, \sum_{i=1}^{j+1} \lambda_i < 0. \tag{5}$$

D_{KY} reflects the fractal dimension (a concept to be recalled below) of the "core" of the attractor, *i.e.* the region of the phase space the most densely visited by the attractor, and it is an upper

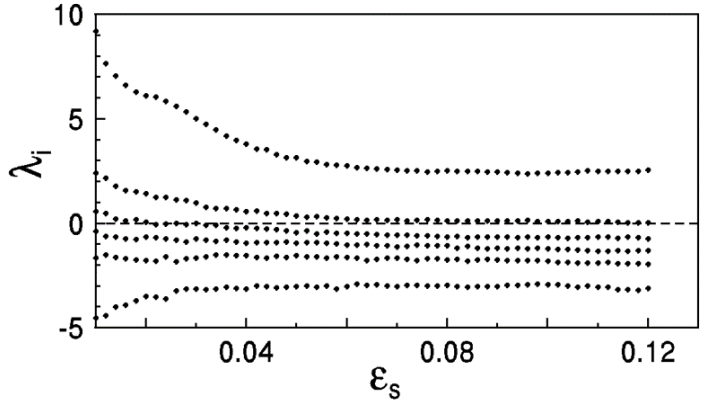

Figure 4: Lyapunov exponents λ_k for a chaotic attractor, from the modified Eckman's algorithm. ϵ_s denotes the characteristic length of the shell. Note the constancy of the exponents λ_k on a large ϵ_s range, and the occurrence of a positive exponent, a zero exponent and several negative exponents such that the sum of exponents is negative. $Al - 2.5\%Mg$ polycrystal loaded at $\dot{\epsilon}_a = 5.56 \times 10^{-6} s^{-1}$. After [63], with permission of the Editor.

bound to the fractal dimension of the attractor [58]. Difficulties in obtaining reliable values for the Lyapunov exponents may arise from two sides. First, the experimental time series may be too short to provide the number of data points required by the algorithms. Second, experimental data may be noisy, so the attractor in the reconstructed phase space is also smeared with noise. Hence, care must be exercised to make sure that the attractor is robust in the sense that the extent of noise in the phase space remains small as compared with the total extent of the attractor. To this aim, noise reduction techniques such as the Singular Value Decomposition of the trajectory matrix are useful, as already mentioned above [22, 52].

3.1.4 Self-similarity and correlation dimension

The self-similarity of the attractor is characterized by its fractal dimension D_f [59]. An estimate of D_f is usually obtained via the box-counting method. In the latter, the attractor is covered by boxes of characteristic linear size δr and the number $N(\delta r)$ of boxes visited by the attractor is counted. For a conventional homogeneous fractal object visiting all boxes of same size δr with the same probability $p(\delta r)$, D_f describes, through the scaling relation $N(\delta r) \propto \delta r^{-D_f}$, how $N(\delta r)$ increases in the limit of small δr. Since the attractor does not fill uniformly the phase space, D_f is less than the embedding dimension d, and it is generally a non-integer. Thus, the lowest integer part of $(D_f + 1)$ is often taken as a lower bound of the embedding dimension required for a proper dynamical description of the system. However, a more convenient method for characterizing the self-similarity of the attractor is its correlation dimension ν, which has been shown to be an upper bound for the fractal dimension [60]. The correlation integral is defined as the fraction of the pairs of points $(\mathbf{X}_i, \mathbf{X}_j)$ of the attractor whose distance is less than a specified value r:

$$C(r) = \frac{1}{N_p} \sum_{i,j} H(r - |\mathbf{X}_i - \mathbf{X}_j|) \tag{6}$$

where $H(.)$ is the Heaviside function and N_p is the number of pairs used in the sum. The self-similar structure of the attractor is reflected in the scaling relation $C(r) \sim r^{\nu}$, where the correlation dimension ν describes how the correlation integral decreases in the limit of small r. In practice, ν is obtained by using the Grassberger-Procaccia algorithm [60]. As the embedding dimension d is increased, the number of false neighbors decreases (if the attractor is self-similar)

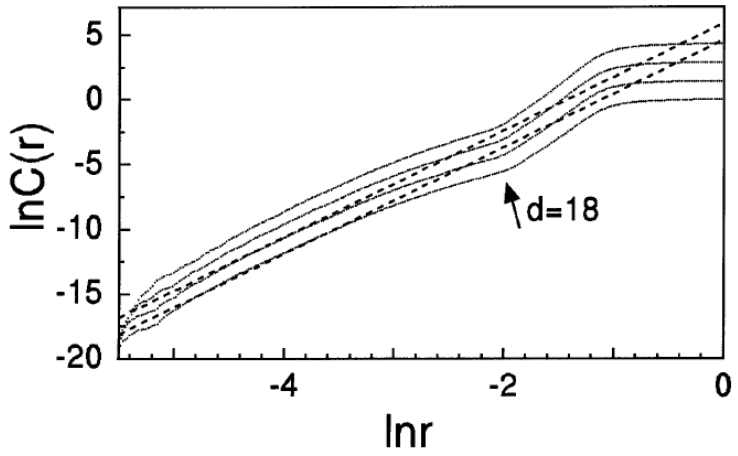

Figure 5: $Al-2.5\%Mg$ polycrystal loaded at $\dot{\epsilon}_a = 5.56 \times 10^{-6} s^{-1}$. Correlation integral showing convergence in the range $-5 \leq lnr \leq -3$, for embedding dimensions $d = 18$ and correlation dimension $\nu = 4.15$. For clarity, the curves corresponding to $d = 15 - 17$ have been shifted upwards with respect to $d = 18$. Dashed lines are plotted as guides to the eye. After [63], with permission of the Editor.

and, if r is not too large, the slope $\ln C(r)/\ln r$ tends to a constant value ν, taken as the correlation dimension. Due to limited length of the time series and noise superimposed on the signal, the scaling regime is also looked for at not-too-small values of r, and only for some larger than ν values of the embedding dimension, as illustrated by Fig.5.

The existence of a finite correlation dimension is not by itself a sufficient reason for the time series to be of chaotic origin, as it does not prove the sensitivity to initial conditions in the phase space. Indeed, it can also arise from a power law stochastic process (see [55] and references therein). However, combining the oscillatory nature of the time series and the boundedness of the attractor with the existence of both a finite correlation dimension and a positive Lyapunov exponent provides a convincing set of arguments enabling to reach safely this conclusion. An additional compelling check is the consistency of the independently calculated Lyapunov and correlation dimensions, D_{KY} and ν, which both provide an upper bound to the fractal dimension of the attractor.

3.2 Scale invariance and self-organized criticality

In a chaotic system, the attractor is bounded in the phase space and the dynamics is described by a small number of independent variables, as recalled above. In contrast, for SOC dynamics (and also for random systems), the orbit fills up an infinite dimensional phase space. Similarly, and again in contrast with the roughly bell-shaped distributions of events size in a chaotic regime, the statistical distribution of events $p(x)$ in SOC dynamics (with x being a generic notation for the magnitude or duration of bursts of activity) exhibits power-law behavior, *e.g.* $p(x) \propto x^{-a}$, which implies the lack of a characteristic event size. Indeed, the functional relation $p(kx) \propto k^{-a} p(x)$ displays scaling symmetry, meaning that the distributions are self-similar in this scaling operation. The terms "self-organized criticality" point at the spontaneous propensity of a driven system to organize itself in the close vicinity of a critical threshold for bursts of activity occurring on a short time scale, at least a much shorter time scale than the slow time scale of the driving force, without any dedicated external tuning. As this property holds all over the spatial extent of the system, it implies the existence of long-range spatial correlations throughout the system. One standard example of such a behavior is the sand-pile model originally formulated by Bak and co-workers to explain the Gutenberg-Richter law, another well-known power law

statistical distribution describing the occurrence of earthquakes [32]. The sand-pile builds up by the continuous addition of sand particles driven by gravity, and its slopes evolve naturally to a critical angle where sand avalanches of all sizes occur (at least in the model if not in the real world, see [33]), also leading to power law statistical distributions of avalanches. From the results to be described below, it will appear that jerky flow provides a convenient laboratory example of SOC in a certain range of high applied strain rates.

3.3 Multifractality

Homogeneous fractality, or simply fractality, and the concept of a fractal dimension have been recalled above in Section 3.1.4. In that Section, which was devoted to self similarity from the example of a chaotic strange attractor in a d-dimensional phase space, it was assumed that the probability for the orbit to visit a d-dimensional box of linear size δr does not depend on the location of the box on the attractor. However, it appeared from the example of the Lyapunov dimension of the attractor that the probability of visiting the core of the attractor is larger than the probability of visiting its surroundings [58]. Thus, it is appropriate to consider a non-uniform probability of visiting the covering boxes [34]. Let us denote by n_j the number of times the orbit visits the jth box of linear dimension δr. The probability of visiting that box is $p_j(\delta r) = n_j / \sum_{k=1}^{N(\delta r)} n_k$, where $N(\delta r)$ is the total number of boxes of size δr needed to cover the attractor; $p_j(\delta r)$ can be considered as a measure associated with that box. It scales as $p_j(\delta r) \propto \delta r^{\alpha}$ in the limit of small δr, where α belongs to a range of values corresponding to different subsets of the attractor. In this relation, α reflects the local behavior of the measure: the smaller the exponent α, the more singular its local behavior. Therefore, α goes by the name of "singularity index" or "singularity strength" of a subset. Since different parts of the attractor have different visiting probabilities, they also have different fractal dimensions. Then, the homogeneous scaling relation $N(\delta r) \propto \delta r^{-D_f}$ defining D_f generalizes to $N_\alpha(\delta r) \propto \delta r^{-f(\alpha)}$. Here $N_\alpha(\delta r)$ is the number of boxes of size δr needed to cover the subset of singularity strength α, and $f(\alpha)$ is the fractal dimension of that subset. The more heterogeneous the attractor, the larger the range of α values. Hence, the degree of heterogeneity of the attractor is fully captured by the range of multifractality $\theta = \alpha_{max} - \alpha_{min}$, where α_{max} and α_{min} are the extreme values of α, all of them clearly visible in Fig.6. Of course, $\theta = 0$ for a homogeneous fractal. To sum up this presentation, the multifractal analysis essentially allows to uncover the presence of correlations in a subset of events through their scaling behavior, and to characterize the heterogeneity of the scaling properties over a range of subsets. Although we used for convenience a heterogeneous chaotic strange attractor in a d-dimensional space as the object to analyze, the multifractal analysis of heterogeneity does not depend on the nature of the dynamics it represents. Actually, the analysis applies to any set of singular events belonging to an embedding space, irrespective of the dynamics. In the present work, the simplest heterogeneous sets of events were used, namely the sets, embedded in one-dimensional time series, of time intervals δt with a measure based on the non-zero absolute magnitudes of the stress derivative: $\psi = |d\sigma/dt|$, because they aptly represent the plastic activity bursts occurring during time intervals δt.

For computational stability reasons, $f(\alpha)$ is usually determined by using averaged quantities obtained from the partition functions $S_q(\delta r)$ [61]

$$S_q(\delta r) = \sum_{j=1}^{N(\delta r)} p_j^q(\delta r). \tag{7}$$

Defining the new measure $\mu_i(\delta r, q) = p_i^q(\delta r)/S_q(\delta r)$, the values of $(\alpha, f(\alpha))$ are then determined

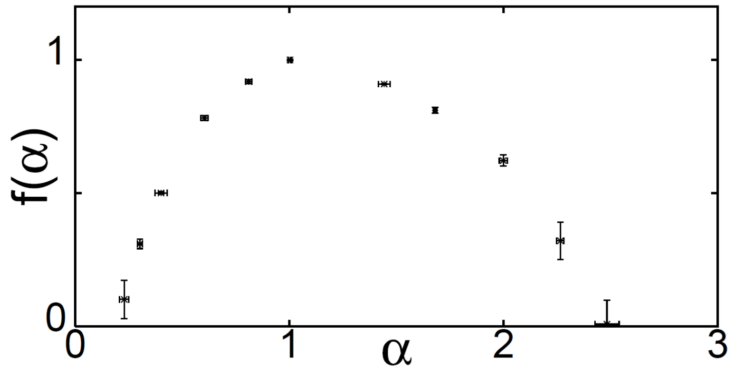

Figure 6: Multifractal spectrum $(\alpha, f(\alpha))$ at applied strain rate $\dot{\epsilon}_a = 1.39 \times 10^{-3} s^{-1}$ in $Al - 2.5\% Mg$, $q \in [-5, +5]$. After [62], with permission of the Editor.

for each q from the scaling relations:

$$\sum_{i=1}^{N(\delta r)} \mu_i(\delta r, q) ln p_i(\delta r) \sim \delta r^{\alpha}, \tag{8}$$

$$\sum_{i=1}^{N(\delta r)} \mu_i(\delta r, q) ln \mu_i(\delta r, q) \sim \delta r^{f(\alpha)}. \tag{9}$$

Different subsets of events become dominant as the exponent q is varied. Large positive q values allow to focus on the smallest α values (large p_is), whereas large negative values focus on the region where α is the largest (small p_is). These extreme regions are those where the density exponent $f(\alpha)$ is the smallest. Between these two extremes, a smooth continuous spectrum of singularity exponents α versus their densities $f(\alpha)$ is obtained, as shown in Fig.6. For $q = 0$, $f(\alpha)$ is simply the fractal dimension D_f of the attractor, which also turns out to be the largest possible $f(\alpha)$ value.

4 Experimental results

The first statistical and dynamical analyses of the macroscopic plastic bursts in jerky flow were made in single crystals [38, 54], and Ladislas contributed to both. The observation of slip band traces onto the surface of the samples being easier in single crystals, it was conjectured that the information thus provided could be of some help in the interpretation of jerky flow, and it was assumed that this interpretation might be simpler than in polycrystals, which ended up being true, but did not help much in the analysis. Similar analyses of the stress serrations and localization bands were shortly after conducted in our group in polycrystals [39, 52], with the additional help of multifractal analysis [62, 63]. In the mean time, research was conducted on the collective behavior of dislocations in uniform plastic flow by other groups [51, 64, 65], mainly on the basis of statistical studies of the associated AE. The comparison of the results was challenging, and it prompted us to launch new experiments on jerky flow in which both the macroscopic plastic bursts associated with stress serrations and the mesocopic plastic events associated with AE could be simultaneously monitored and studied using statistical and multifractals analyses [18, 66].

Perhaps the most easily perceived hints that different types of behavior of the PLC effect correspond to specific dynamical regimes came from statistical analyses of the stress drops. The first results obtained for both $Al - Mg$ single and polycrystals showed that the distributions of stress drop magnitudes were roughly bell-shaped at low and medium strain rates, then became

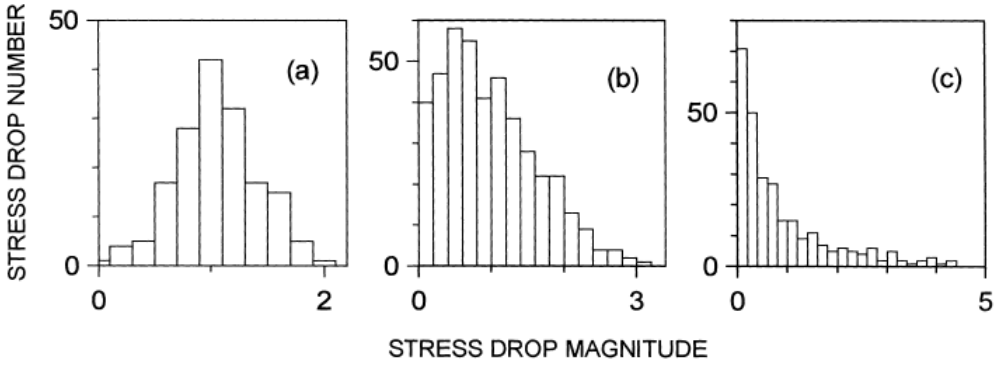

Figure 7: Examples of histogram shapes for room temperature deformation : (a) polycrystalline specimen of $Al-3\%Mg$ alloy, $\dot{\epsilon}_a = 1.3 \times 10^{-5} s^{-1}$; (b) single crystal of $Al-4.5\%Mg$ alloy, $\dot{\epsilon}_a = 1.3 \times 10^{-5} s^{-1}$; (c) polycrystalline specimen, $Al-3\%Mg$, $\dot{\epsilon}_a = 6.1 \times 10^{-4} s^{-1}$. After [39], with permission of the Editor.

more and more asymmetrical as the strain rate was increased, and shifted to power-laws at high strain rates [38, 39, 67], as illustrated in Figs. 7(a) and 7(c) for an $Al-3\%Mg$ alloy. Similar transitions occurred when temperature was decreased [39]. These transitions correspond to the well-established C, B, and A behavior types in polycrystals. Such types are not as clearly defined in single crystals, where perfectly regular serrations leading to symmetric bell-shaped histograms were not observed (cf. Figs.7(a) and 7(b)). This observation came as a fair confirmation of the prospectively assumed role of spatial coupling in the collective dynamics of dislocations. On the whole, the power-law scaling of stress serrations led to conjecturing SOC at high strain rates. Evidence for quasi-randomness was found at low strain rates, and deterministic chaos at medium strain rates, first in single crystals of copper alloys $Cu-Al$ [54, 55], then in polycrystalline $Al-Mg$ [52, 62, 63, 68]. Some details of the quantitative studies of deformation curves, which successfully provided significant insights into the self-organized nature of the PLC effect, even without resorting to finer experimental techniques, are presented below in Sections 4.2 and 4.3.

4.1 Single crystals

The first attempt at checking if the stress time series could be of chaotic origin was undertaken in [54]. The analysis was carried out on experimental stress signals obtained from $< 111 >$ single crystals of $Cu-14\%Al$ loaded under the applied strain rate of $3.34 \times 10^{-4} s^{-1}$ at a temperature of $294°K$. Twelve files of 6144 points sampled at a rate of 242 points per second, corresponding to a kind of Stage I deformation with one active slip system and a rather low work-hardening coefficient ($80\,MPa$) were analyzed. The analysis used the Grassberger-Procaccia algorithm, whereby a finite correlation dimension $\nu \approx 2.3$ was found. However, no Lyapunov exponent was calculated, and the results were taken as a mere indication of a possibly chaotic regime. Limitations of this work came out of the shortness of the data sets, which in addition often contained a high level of noise.

For this reason, experiments on $Cu-10\%Al$ having produced larger and cleaner files were used in [55]. The single crystal samples oriented for easy glide were deformed at a temperature of $620°K$. The sampling rate was $20\,Hz$. In the domain of occurrence of the PLC effect, three files containing 4×10^4, 2×10^4, and 1.2×10^4 points were recorded at strain rates $3.3 \times 10^{-6} s^{-1}$, $1.7 \times 10^{-5} s^{-1}$, and $8.3 \times 10^{-5} s^{-1}$, and labeled below respectively l, m and h. Offering a wide range of strain rates and reasonably long time series, they provided a suitable basis for the

analysis of the underlying dynamics. The methods used and the results obtained were very similar for the low and medium strain rate files l and m. In both cases, the distribution of stress drops was peaked, with a single peak for the l data and two peaks in the m case. Here, we illustrate the main results with the m file: a scaling region was found in the correlation integral $C(r)$ over two orders of magnitude for a delay time $\tau = 20$, with the slopes $lnC(r)/lnr$ converging as the embedding dimension approached $d = 9$. The resulting correlation dimension was $\nu \approx 2.7$. The analysis proceeded with the calculation of the Lyapunov spectrum, using the modified Eckmann's algorithm. For the embedding dimension $d = 5$ and the delay time $\tau = 2$, stable positive and zero exponents (λ_1, λ_2) were obtained over a sufficiently large shell. From the existence of a finite correlation dimension and of stable positive and zero Lyapunov exponents, it was therefore concluded that both time series were of chaotic origin.

In the high strain rate file h, the statistical distribution of stress drops showed a scaling form: $p(\Delta\sigma) \sim \Delta\sigma^{-\alpha}$ with an exponent $\alpha \approx 1.1$. Similarly, the normalized distribution of the time duration T of the stress drops had the scaling form $p(T) \sim T^{-\beta}$, with $\beta \approx 0.9$. In the absence of characteristic scales, the magnitudes of the stress drops are expected to scale with their durations according to the power law $\Delta\sigma \sim T^{1/x}$. In practice, since time is monitored at finite intervals Δt, there is a distribution of stress drops for each value of T. Thus one can also check for the average magnitudes of the stress drops $< \Delta\sigma >$ as a function of their durations T, in the form $< \Delta\sigma > \sim T^{1/x}$, and then obtain an exponent value $x \approx 1.25$. The three scaling exponents α, β and x should be related to each other through $\alpha = 1 + x(\beta - 1)$ [33]. This relation was quite well satisfied, showing that the scaling statistics of the high strain rate file h were fully consistent. Of course, they were in sheer contrast with the quasi-Gaussian statistics of the low and medium strain rate files l and m. To check if the drift in the statistics translated to a drift in the underlying dynamics, the Lyapunov spectrum of exponents was calculated and attempts were made at obtaining a converged correlation dimension. It appeared that only negative values of the Lyapunov exponents could be found, whatever the choice of the embedding dimension and delay time, and that no converged value of the slope $lnC(r)/lnr$ of the correlation integral could be obtained. Clearly, all these results are in marked contrast with those obtained for the low and medium strain rate files l and m. Hence, there are strong indications that a crossover occurs in the underlying dynamics as the strain rate is increased. Actually, all the features associated with the h file are reminiscent of SOC-type dynamics [32, 33], in which events of all magnitudes occur, with power law distributions. Indeed, as any disturbance grows as a power law in time, no positive Lyapunov exponent can be found. There is no compact attractor in the reconstructed phase space, which is instead uniformly filled up by the trajectories, and a finite correlation dimension is therefore absent. Thus, the identified crossover clearly signals a shift from chaotic to SOC-type dynamics. Physical reasons for this change of paradigm will be provided below in Section 5.

4.2 Polycrystals

4.2.1 Cold-rolled Al – 2.8%Mg

In reference [52], the $Al - 2.8\%Mg$ polycrystalline samples had been cold rolled and annealed at $460°C$ for 3 hours, which yielded an average grain size of $250\,\mu m$. The tension tests were carried out at room temperature with an imposed constant strain rate of $6.67 \times 10^{-5} s^{-1}$. The data were sampled at a frequency of $20\,Hz$ and contained a total of 28254 points. The accuracy in the load measurement was up to $10^{-6}\,MPa$. Comparing with the 6144 data points and $10^{-2}\,MPa$ accuracy of the files analyzed in [54] suggests that the level of noise had been much reduced and that fairly long time series were available. In addition, the noise level was further reduced by using the Singular Value Decomposition of the trajectory matrix. It appeared that, starting from its sixth principal value, the ratio with respect to the first and largest one had decreased by at least two orders of magnitude. Thus, noise-reduced time series were obtained by keeping only the first six principal components and back rotating the trajectory matrix to its canon-

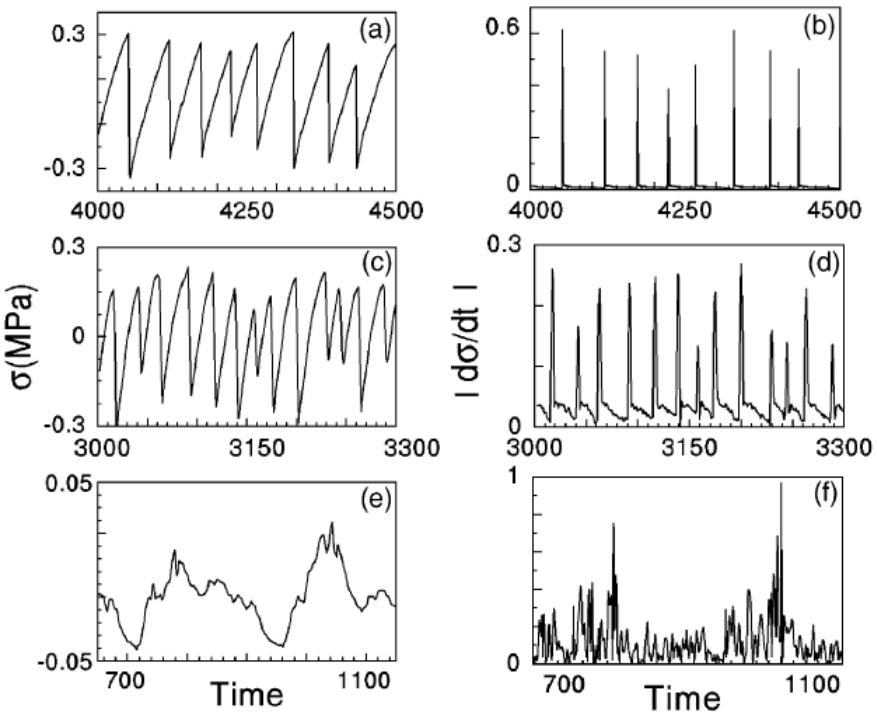

Figure 8: $Al-2.5\%Mg$ polycrystal, as-received colled-rolled microstructure r. Left: Stress time series. Right: Corresponding absolute values of the stress time derivative $\psi = |d\sigma/dt|$. The applied strain rate increases from top to bottom: $(a,b)\,\dot{\epsilon}_a = 5.56 \times 10^{-6}$, $(c,d)\,2.78 \times 10^{-4}$ and (e,f) $5.56 \times 10^{-3} s^{-1}$. After [63], with permission of the Editor.

ical space. A projection of the attractor in the noise-reduced subspace spanned by the three first eigenvectors is shown in Fig.2. The dynamical analysis used the Grassberger-Procaccia algorithm for checking the existence of a finite correlation dimension in both the original and noise-reduced files. In the latter, the slope $ln(C(r))/ln(r)$ of the correlation integral converged to the correlation dimension $\nu = 3.05$ in a range of intermediate distances r as soon as the embedding dimension d reached $5-10$. For the uncured time series, the calculations yielded $\nu = 3.2$ when d reached 5, rather close to the cured case, which suggests that the influence of noise was limited at intermediate distances. The modified Eckmann's algorithm was used for computing the spectrum of Lyapunov exponents. Since the number of data was fairly large, the complete spectrum and, consequently, the Lyapunov dimension could be determined. In both the original and noise-reduced files, a positive and a zero exponent were found. The positive exponent and Lyapunov dimension were ($\lambda_1 = 1.0$, $D_{KY} = 3.027$), and ($\lambda_1 = 0.62, D_{KY} = 3.023$) for the original and noise-reduced files, respectively. Thus, the evidence for chaos was strong, as follows from the existence of a finite correlation dimension and the presence of stable positive and zero Lyapunov exponents. In addition, the correlation and Lyapunov dimensions were close and fully consistent in both the original and noise-reduced files. Further, it is interesting to note that the positive exponent λ_1 is much larger in the uncured file, which suggests that all fluctuations introduced by noise induce larger stretching of small initial difference vectors, consistent with the linear instability of the strange attractor.

4.2.2 Al – 2.5%Mg with different microstructures

In contrast with reference [52] discussed above, which was only focused on the analysis of a single experiment, the papers [62, 63] provided an overall point of view on the non-linear dynamics of jerky flow in polycrystals. Connections were made between the initial microstructure of the

material, the serration types, the statistics of the plastic activity events and the underlying dynamical regimes as the experimental conditions were varied. This was made possible by carrying out a series of tensile experiments on polycrystalline $Al-2.5\%Mg$ samples with different initial microstructures over a wide range of strain rates. Three sets of samples were prepared from a cold-rolled sheet. The first set, labeled r, was extracted from the as-received material. The grain morphology was anisotropic, showing an aspect ratio of 5 and an average grain size of $30-40\,\mu m$ along the rolling direction. A second group, labeled a, was annealed for $4h$ at $593\,^{\circ}K$ and quenched in water, which produced a less anisotropic morphology with an aspect ratio of 3 and an average grain size of about $50\,\mu m$ in the same direction. The third group, labeled aa, was subjected to an additional $3h$ annealing at $733\,^{\circ}K$ before water-quenching. This treatment produced a nearly equiaxed structure with a large average grain size of about $1\,mm$. The tensile axis of the extracted flat samples was parallel to the rolling direction. The tests were carried out at room temperature, and eight values of the applied strain rate were selected in the range $5.56\times10^{-6}s^{-1}$ to $1.39\times10^{-2}s^{-1}$. The PLC effect was observed throughout this range. A sampling rate of $20\,Hz$ was selected, except for the highest applied strain rate where a $200\,Hz$ frequency was adopted. Three of the obtained stress vs. time and stress rate vs. time curves are shown in Fig.8 for the r microstructure.

The correlation dimension and Lyapunov spectrum were both calculated and provided unambiguously positive results in terms of chaotic dynamics for all three microstructures, but in shrinking ranges of strain rates as the memory of the cold-rolled state decreased. Indeed, if the lower bound of chaotic behavior was the smallest strain rate, $\dot{\epsilon}_a = 5.56\times10^{-6}s^{-1}$, for all microstructures, its upper bound was found to shift towards lower strain rates as the microstructures went from r to a, then to aa. For the aa microstructure, chaos was detected only at the lowest strain rate. In addition, the chaotic domain was found to lay inside the domain of type B serrations, and to coincide with the domain of bell-shaped distributions for bursts of plastic activity. Its unambiguous identification became impossible as soon as these distributions became asymmetrical, even if the bands looked like type B bands. All results were similar in terms of correlation dimension and Lyapunov spectrum. Stable positive and zero Lyapunov exponents were found, and the Lyapunov dimension was systematically calculated. The analyses are illustrated in Figs.4 and 5 for the cold-rolled state r at the lowest strain rate, with the values $\nu = 4.15$ and $D_{KY} = 4.2$, very close to each other, confirming that the time series were indeed of chaotic nature.

In the statistical analysis, the bursts of plastic activity were rendered by the modulus $\psi(t)$ of the time derivative of $\sigma(t) : \psi(t) = |d\sigma/dt|$ (see Fig.8). Since the results were essentially similar in all three microstructures, they are again illustrated here with the results of the as-received set r. As already mentioned, peaked distributions $p(\Delta\psi)$ and $p(\Delta t)$ of the bursts magnitudes $\Delta\psi$ and durations Δt were observed in the chaotic regime, indicating the existence of characteristic values. As the applied strain rate $\dot{\epsilon}_a$ was increased, the distributions became asymmetrical and secondary peaks tended to show up in the mid-region of $\Delta\psi$. With further increase in $\dot{\epsilon}_a$, fully asymmetrical distributions were obtained in the form of power-laws $p(\Delta\psi) \sim \Delta\psi^{-a}$. At strain rate $\dot{\epsilon}_a = 5.56\times10^{-3}s^{-1}$, the scaling exponent was $a \approx 1.5$ over more than one order of magnitude of $\Delta\psi$. Similarly, the distributions of burst durations were also conveniently fitted by the power-law $p(\Delta t) \sim \Delta t^{-b}$, with $b \approx 3.2$. In addition, the conditional mean $<\Delta\psi>$ of $\Delta\psi$ (*i.e.* the mean of $\Delta\psi$ at time t, given the information at time $(t-\Delta t)$) scaled as $<\Delta\psi> \sim \Delta t^x$ with $x \approx 4.2$. Thus, the consistency relation $b = 1 + x(a-1)$ between the scaling exponents (a, b, x) [33] was found to be quite well satisfied. All the above high strain rate results are fully compatible with SOC dynamics. Summarizing the results obtained for all files (r, a, aa), the SOC dynamics domain is insensitive to the microstructure, at least in this alloy. It only requires a sufficiently high strain rate, and coincides with the domain of continuously propagating type A bands. In contrast, the domain of chaotic dynamics and the transition region from chaos to SOC are microstructure-sensitive in a coupled manner. At a certain low or medium strain rate, the

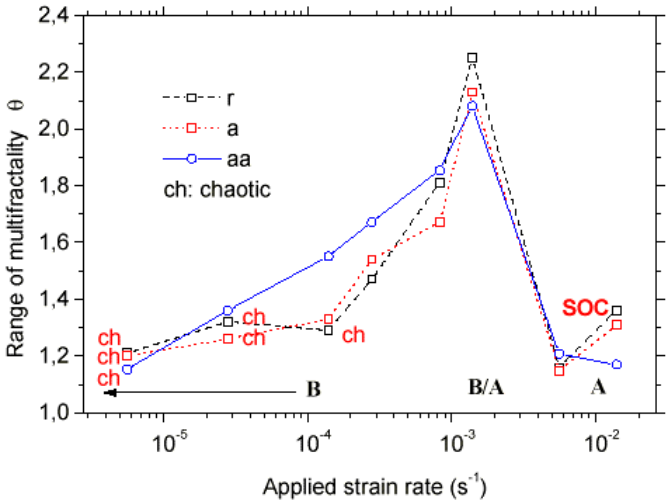

Figure 9: Multifractal range θ vs. applied strain rate $\dot{\epsilon}_a$. (r, a, aa) refer to as received, annealed and doubly annealed microstructure in $Al-2.5\%Mg$ polycrystal. Regions of chaotic type B and SOC type A bands are marked. After [63], with permission of the Editor.

existence of chaos requires a sufficiently hard microstructure with sufficiently strong obstacles to dislocation motion, *e.g.* sufficiently dense forest dislocations or/and sufficiently small grain sizes, and all the more so that the applied strain rate $\dot{\epsilon}_a$ is higher. Conversely, the extent of the crossover region from chaos to SOC progressively increases toward lower strain rates as the microstructure evolves from cold-rolled r to doubly annealed aa. In this range, the distributions $p(\Delta\psi)$ are rather complex, neither power-laws nor symmetrical peaked, and suggest heterogeneity of the dynamics.

Hence, a multifractal analysis was carried out on all samples, not only in the crossover region, but also in the entire range of strain rates, and the multifractal spectra $(\alpha, f(\alpha))$ were calculated in all cases. The formalism described in Section 3.3 applies when understanding the local probabilistic measure, $p_j(\delta t)$, of the signal ψ as defined by the sum of the ψ_k values within the j-th δt-box of the time grid, normalized by their sum over the entire time interval analyzed. A plot of the spectrum for the file r corresponding to the strain rate $\dot{\epsilon}_a = 1.39 \times 10^{-3} s^{-1}$, for which the range of multifractality θ is maximum, is shown in Fig.6. The dependence of θ on the driving parameter $\dot{\epsilon}_a$ is shown in Fig.9 for all three microstructures. In the r and a materials, θ keeps relatively low values at both low/medium and high strain rates, which reflects a relatively high degree of homogeneous self-similarity of the underlying dynamics. At low/medium strain rates, this is due to the homogeneously Gaussian character of the distributions of plastic bursts, and at high strain rates, to the homogeneous scaling character of these distributions. Note that at low and medium strain rates, θ is substantially higher in the aa samples, due to the heterogeneity of distributions mixing asymmetry and secondary peaks in that case. The main feature in the figure is clearly the sharp peak highlighting the crossover region from chaos to SOC-type dynamics. The high level of multifractality reflects the strong spatial heterogeneity of the plastic activity in this range. The figure also illustrates clearly the sensitivity of the chaotic regime to the microstructure at low/medium strain rates, and the more universal character of SOC at high strain rates, at least in this alloy.

Similar statistical and dynamical analyses of the plastic bursts in jerky flow had been carried out in $Cu-Al$ single crystals, as recalled in Section 4.1, even if no multifractal analysis was attempted. Given that the obstacles to dislocation motion are different, it is remarkable that similar conclusions were reached, although the numbers were quite different. The correlation dimension $\nu \approx 2.7$ found at low strain rates in the chaotic regime was much smaller than the

value $\nu \approx 4.15$ measured in the $Al-Mg$ polycrystals which implies that fewer degrees of freedom are required in single crystals than in polycrystals for the description of the dynamics of jerky flow, which comes as no surprise. The SOC dynamics observed at high strain rates had exponent values typically around unity, again much lower in single crystals than in polycrystals. Finally, the faster decay of plastic bursts distributions in polycrystals implies smoother evolutions in time and a smaller range of time scales involved in their dynamics.

4.3 Acoustic Emission monitoring

As already suggested, the statistics of the AE associated with the small plastic events involved in macroscopically uniform flows were studied in parallel to our serration statistics in some pure crystalline solids, such as ice and copper [51, 64, 65]. In contrast to conventional wisdom, which had it that uniform plastic flow derives from randomness averaging out dislocation slip in systems containing large numbers of dislocations, the observed AE was not described by Gaussian statistics, but rather by power-law distributions, which bears evidence to the intermittent scale-invariant character of stable uniform plasticity. Thus, it seemed interesting to use a similar approach in the case of macroscopically unstable plastic flows, and to extend the analysis of the plastic instability to the scale pertaining to the AE.

Experiments were carried out to simultaneously investigate the macroscopic plastic bursts associated with stress serrations and the mesocopic plastic events associated with AE, using statistical and multifractals analyses [18, 66]. The samples were cut from a cold-rolled sheet of polycrystalline $Al-3\%Mg$ alloy, annealed at $400\,^{\circ}C$ for $2\,h$, and quenched into water. The tensile tests were conducted at room temperature in a wide range of applied strain rates $\dot{\epsilon}_a$, from $2\times10^{-5}s^{-1}$ to $6\times10^{-3}s^{-1}$. The sampling time of the stress time series varied with $\dot{\epsilon}_a$, from $500\,ms$ at the lowest strain rate to $4\,ms$ at the highest one. As a result, all records contained a similar amount of data, somewhere between 15000 to 50000 data points. The accuracy of the load measurement was at least $0.01\,MPa$. The sampling rate of the AE recording system was $4\,MHz$. As the test lasted hours at low strain rates, the AE signal was not "continuously" recorded at this frequency. Instead, series of AE events ("hits") were extracted "in real time" during deformation. As recalled in Section 2, the system picks out an acoustic event when the signal exceeds a pre-set threshold voltage, then measures such characteristics as its amplitude, duration and energy. The event is considered to have ended if the acoustic signal remains below the threshold voltage for a duration exceeding the HDT. A certain dead time follows, during which no hit is searched for, in order to filter out sound reflections from the sample surfaces.

In addition to the common stress serration patterns and statistics (see the histograms in Fig.10), the type B and type C stress-strain curves also displayed usually neglected smaller-scale fluctuations [69, 70]. The amplitude $\Delta\sigma$ of the large stress drops occurring beyond a critical strain ϵ_{cr}, and considered a signature of type C behavior, was in the range $5-15\,MPa$ [18, 66]. In contrast, the small stress drops occurred almost from the onset of plastic deformation. Their amplitude increased progressively to $1-2\,MPa$, but kept sweeping the whole range down to the noise level of the measurements ($\approx 0.01MPa$). In type B conditions, the first part of the deformation curve, below ϵ_{cr}, also displayed such low-amplitude events, although in the form of smooth undulations. However, these events could not be clearly separated from the typical type B serrations beyond ϵ_{cr}. When $\dot{\epsilon}_a$ was further increased (type A behavior), no characteristic scale of serrations could be detected and the separation into small and large events was impossible. Applying the statistical analysis separately to the group of small type C events, scaling behavior of the stress drops probability distribution was found with a dependence $p(\Delta\sigma)\sim\Delta\sigma^{-a}$ valid in a wide range covering about 2 orders of magnitude of $\Delta\sigma$ (see Fig.11). The exponent a varied in the range $1-1.5$ depending on the sample, similar to the exponents observed for type A stress drops at high strain rates. Power-law dependence was also verified for

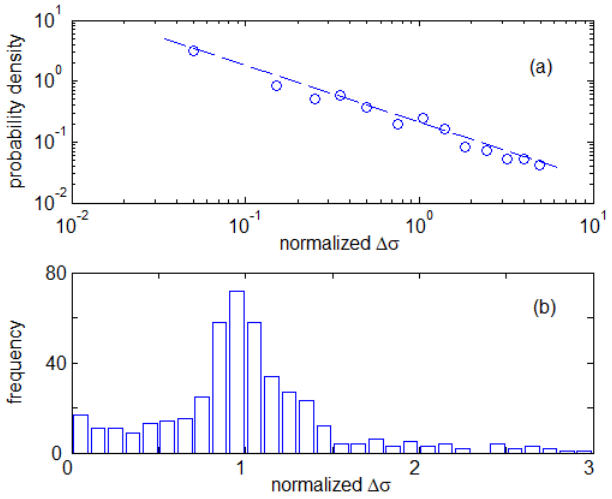

Figure 10: $Al-3\%Mg$ polycrystal. (a) Probability density of the normalized amplitude $\Delta\sigma$ of type A stress drops, $\dot{\epsilon}_a = 2\times10^{-3}s^{-1}$. Scale invariance over two orders of magnitude is observed. (b) Histogram of the distribution of type B stress drops, $\dot{\epsilon}_a = 2\times10^{-4}s^{-1}$, with quasi-Gaussian character. The histogram for the type C stress drops is shown in Fig.11. After [18], with permission of the Editor.

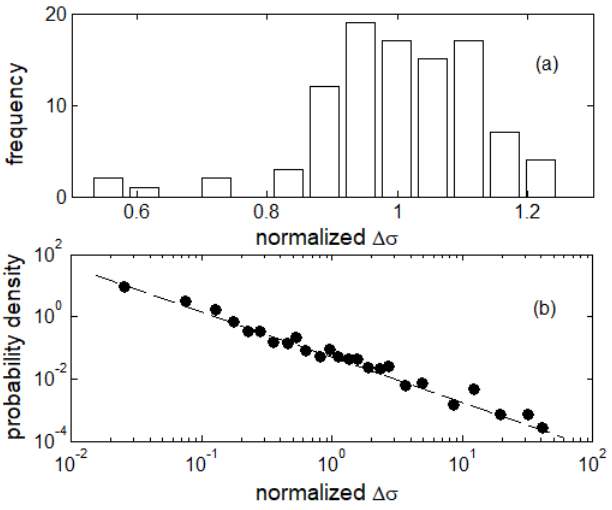

Figure 11: $Al-3\%Mg$ polycrystal (a) Histogram of distribution of stress drops of type C, $\dot{\epsilon}_a = 2\times10^{-5}s^{-1}$. (b) Probability density function for low-amplitude stress drops, $\Delta\sigma < 5MPa$, observed for the same sample in the same time interval. After [18], with permission of the Editor.

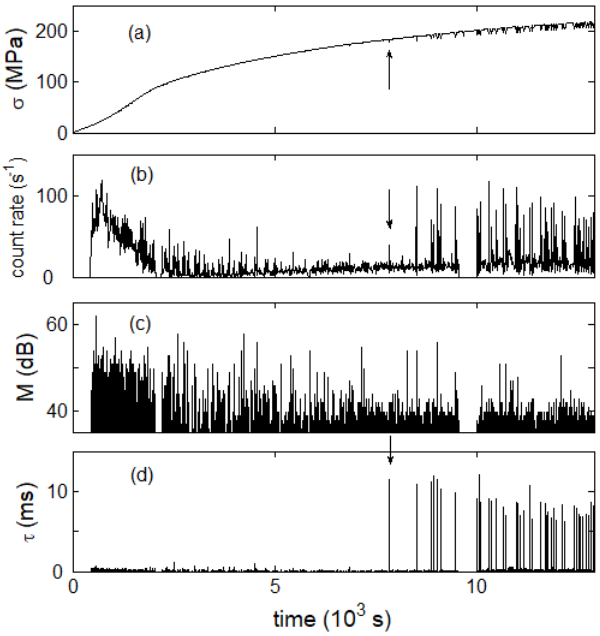

Figure 12: (a) Nominal stress vs. time curve for cold-rolled $Al-3\%Mg$ polycrystal at strain rate $\dot{\epsilon}_a = 2\times10^{-5}s^{-1}$ in the domain of Type C serrations. (b) AE count rate calculated by averaging over time intervals of $10s$; two "silent" intervals correspond to technical stops in AE acquisition. (c) Logarithmic amplitude M of the individual AE events. (d) Respective duration τ of these events. $HDT = 300\mu s$. In all panels, the arrows show the instant in time corresponding to the critical strain ϵ_{cr} for the onset of macroscopic PLC serrations. Note in panel (c) thatthe onset of macroscopic serrations does not affect the range of logarithmic amplitude M of the AE hits. In contrast, bursts in the AE event duration are clearly observed from this point in panel (d). After [18], with permission of the Editor.

the duration probability distribution and the relationship between the amplitude and duration, confirming a scaling character reminiscent of SOC for these small stress drops statistics. Yet and as could be expected despite this small scale behavior, the large stress drops simultaneously observed in the same experiments led to rather symmetrical peaked distributions, in agreement with the typical type C serrations behavior, as Fig.11 shows.

This emerging trend to scaling-type statistics as the scale of the observation is reduced, was further confirmed by the statistical analysis of the associated AE, which monitors even smaller events than the small stress drops. The analysis used the squared value A^2 of the peak amplitude A of the acoustic event, expressed in voltage units. As mentioned in Section 2, A^2 provides a measure of plastic activity by reflecting the energy dissipated by plastic straining in the sample [64]. The main result of this analysis was that the distributions $p(A^2)$ obeyed power laws in all deformation conditions, including the type B and C regimes characterized by peaked distributions of stress serrations. The power laws covered more than two (up to three) orders of magnitude of the variable A^2. The power-law exponent α_{AE} evolved during the deformation process. Depending on the driving rate, it varied between 1.5 and slightly more than 2 at the onset of plastic deformation. During the unstable flow, it took on higher values, ranging roughly from 2 to more than 3. Finally, α_{AE} decreased in the vicinity of necking. This dependence on the microstructure evolution raises the issue of a competition between correlated and random behavior of dislocations (see [71] for a recent development of this aspect).

Further information was looked for by monitoring concurrently the amplitude and duration

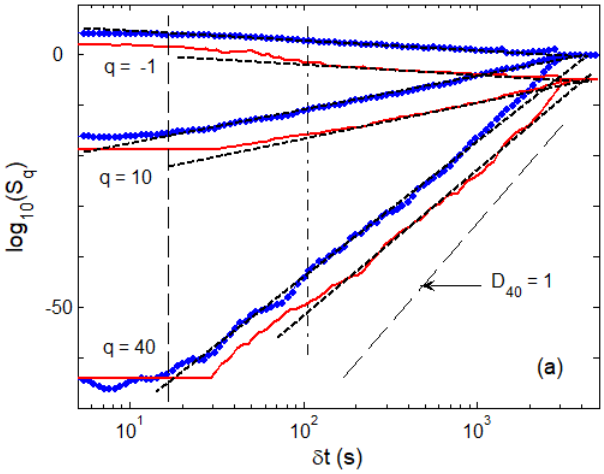

Figure 13: Comparison of partition functions $S_q(\delta t)$ for AE time series (blue dotted lines) and stress time series (continuous red lines) in cold-rolled $Al-3\%Mg$ polycrystal at strain rate $\dot{\epsilon}_a = 2\times10^{-5}s^{-1}$. The bundle of continuous red lines is shifted downwards to improve readability. The dotted lines are guide to the eye. The vertical dashed and dash-and-dotted lines indicate the lower scaling limit for AE and stress time series respectively. Note the much larger range of scaling of AE time series. The oblique dashed line for the (maximum) value $q = 40$ corresponds to the trivial scaling $D_q = 1$. Again for readability, the curves obtained for large negative qs are not shown, due to high data scatter related to noise. After [66], with permission of the Editor.

of the AE hits and the stress drops, first at low strain rates in the range of type C behavior. Perhaps unexpectedly, the occurrence of a stress drop, be it a small-scale drop or a typical large-scale drop occurring beyond the critical strain ϵ_{cr}, did not affect the amplitude range of the AE hits, whereas at the same time, bursts in the AE event duration were observed (see Fig.12). This observation suggests that AE events with a very long duration result from the merger of multiple hits with amplitudes in the usual range. In addition, these long duration AE events were not an exclusive feature of the large serrations: they also occured for the small-scale stress drops observed during macroscopically smooth plastic flow. Therefore, it seems that the same mechanism of plasticity, involving dislocation avalanches in a similar range of size, is at work during both the uniform and the localized plastic flow, and that the large-scale stress serrations are not due to the simultaneous motion of unusually large dislocation ensembles, but to the synchronization of numerous ordinary glide events [66, 72]. When the driving strain rate is increased, the overall AE activity increases, which leads to a globally stronger clustering of AE events, but the correlation between the plastic bursts and the AE duration bursts degrades progressively. Indeed, the large duration bursts accompany only part of the type B serrations, and very few AE bursts are observed during type A instability. The latter is characterized by the absence of characteristic scales of amplitudes and durations for both AE and stress serrations, which testifies to SOC-like behavior over a wide range of scales. Thus, it was conjectured that the role of the synchronization of ordinary glide events in building large scale plastic events subsides as strain rate increases and eventually disappears at high strain rates, to leave the show to SOC.

The above conclusions were further supported by the multifractal analysis. Multifractality was found for both the stress time series and the corresponding AE time series at all strain rates, except for the highest strain rate, $\dot{\epsilon}_a = 6\times10^{-3}s^{-1}$, at which the AE technique becomes unable to resolve individual AE events, due to the increase of the overall AE activity. Significant features were revealed by this analysis. Firstly, the scaling range of the partition functions S_q found for the AE time series was much larger than its counterpart for the corresponding stress

time series, as Fig.13 shows. The extra scaling resulted from a shift of the lower δt limit to values much smaller than the smallest time interval between stress drops. Secondly, the slopes of the $log(S_q) - log(\delta t)$ dependencies kept the same values all over the scaling range, including in its part corresponding to stable flow. It can thus be conjectured that all AE events belong to the same multifractal subset, be they related to stable or unstable plastic flow. Since the same multifractal spectra were found for the AE observed during both the stable (below ϵ_{cr}) and unstable plastic flow (above ϵ_{cr}), it follows that the correlations responsible for their emergence were existing before the occurrence of the macroscopic patterns associated with plastic instability.

To find indications on whether this multifractal character is controlled by correlations in the amplitude or in the time of occurrence of the plastic events, several surrogate time series were analyzed. In a first set, the events amplitudes were kept unchanged but the time intervals between events (*i.e.* the reloading time) were either replaced with random values or kept constant. Such tinkering of the data led to suppressing multifractality altogether. Alternatively in a second set, the times of occurrence of the events were kept unchanged, but their amplitudes were shuffled or replaced with random values, or rendered equal. The effects of such manipulations were dependent on their specifics, but the resulting damage to the scaling behavior was weak (sometimes negligible) in all cases. It was therefore suggested that the correlations in the reloading time prevail over the correlations in amplitude as to the emergence of a multifractal structure and that, in this respect, the amplitudes of AE events are relatively weakly correlated. This conclusion supports the notion that the prevailing correlation mechanism between plastic events stems from the long-range internal stress field and the elastic waves generated by the distortion incompatibilities associated with crystal defects (such as dislocations and grain boundaries) and differently strained regions. The observable, although slight, changes in the multifractal spectra upon amplitude tinkering also suggest the relevance of the short-range interactions between dislocations as a candidate for the spatial coupling mechanisms at work in jerky flow. Such conclusions are supported by Discrete Dislocation Dynamics studies, again inspired by Ladislas Kubin, which suggest that the size of plastic events is influenced by the short-range interactions between dislocations arising from their transport, through dislocation reactions, immobilization or multiplication, *e.g.* due to double cross-slip of screw dislocations [73].

4.4 Acoustic emission: towards finer time scales

The application of the AE technique described above aimed at increasing the measurement sensitivity to abrupt deformation processes. Indeed, perceptible AE can be produced by a small number of collectively moving dislocations, perhaps a hundred or so [46], whereas simple estimates show that large stress serrations involve hundreds of thousands of dislocations. Similarly, the duration of the "elementary" acoustic events may be much less than the duration of macroscopic stress serrations (see Fig.12). Although the statistical and multifractal studies of the previous section conclude to scale-invariance of (rather coarse) AE events, there are few chances that such an analysis could provide complete information on the underlying deformation processes. The above comparisons between the statistics of stress serrations and acoustic events, showed indeed that scale-invariance may not cover the entire range of plastic events, and that self-organization of dislocations may lead to different dynamic regimes, depending on the scale of observation. Spectacular illustrations of such a complexity were also found in the study of the spatio-temporal evolution of the strain-rate fields [42]. Thus it is not surprising that further efforts envisaged AE investigations of the PLC effect at shorter time scales, by either capturing waveforms of individual AE hits in the pre-triggering mode [74, 75], or by applying recently developed methods of continuous AE recording ("data-streaming") [76, 77]. This latter approach is rapidly gaining interest due to the exquisitely detailed information it affords for multiscale analysis. Its application to the PLC effect is still in its infancy, with only a few works com-

pleted so far. The first results presented below illustrate the pursuit of the ideas developed in collaboration and under the guidance of Ladislas Kubin.

4.4.1 Al-Cu polycrystals: structure hidden in the "elementary" AE hits

The first investigation targeted the intrinsic structure of single AE hits over time scales from a few μs to a few ms [78]. As it was *a priori* believed that stress serrations generate intense AE hits, a misconception refuted later (see Section 4.3), type C conditions were looked for, on the one hand in view of the supposedly large magnitude of the corresponding AE events and on the other hand, because there is a large separation time between serrations and virtually no spatial correlation between the corresponding PLC bands. Tensile tests were carried out at room temperature on polycrystalline samples of an $Al-Cu$ alloy (AA2024) with a $57mm$ gauge lengh and a $12.5 \times 2.1\, mm^2$ cross-section, with the nominal strain rate varying from $2.9 \times 10^{-5} s^{-1}$ to $2.9 \times 10^{-2} s^{-1}$. The AE was found at all strain rates, but the multifractal analysis was only carried out at $\dot{\epsilon}_a = 2.9 \times 10^{-4} s^{-1}$, *i.e.*, close to the lower boundary of plastic instability. Individual waveform samples of $2.5\, ms$ duration, containing 10000 data points, were obtained using the pre-triggering mode. This technique is based on continuous saving and erasing of a certain number of readings in a buffer memory, until the AE voltage exceeds the preset threshold and triggers the recording of an AE event. This continuous buffering avoids cutting-off the front of the hit. The AE signal was captured using a piezoelectric sensor with a flat frequency band in a range from 100 to $600kHz$ and sampled at a frequency of $4MHz$.

Typical examples of waveforms associated with stress serrations are presented in Fig.14. It can be seen that the signals vary from isolated decaying bursts illustrated in Fig.14 (a) to chains of multiple bursts, as displayed in Figs.14 (b) and (c). Multifractal analysis was applied to check whether or not such complex waveforms reflect correlated temporal structures. As the continuously recorded AE signal, $V(t)$, is sampled at a constant frequency, the probabilistic measure was defined as described in Sec.4.3 for the deformation curves, also recorded at a constant frequency. Therewith, two choices were probed for the definition of the analyzed signal $\phi(t)$: $\phi(t) = V^2(t)$ and $\phi(t) = |V(t)|$. Both provided compatible results. Obviously, the signal in Fig.14 (a) does not possess self-similar structure, as it comprises two distinct scales corresponding to a short burst followed by decaying oscillations and a low-amplitude background. Some traces of scaling have been detected, though, thus indicating that the visibly noisy component may contain a contribution from correlated deformation processes. In contrast, scaling behavior was clearly present in the complex waveforms shown in Fig.14 (b) and (c), over time intervals covering from two to almost three orders of magnitude of the grid box length, δt, from several μs to almost $1\, ms$. The corresponding $f(\alpha)$ spectra are plotted in Fig.15. In discussing these results, it should be borne in mind that an AE signal is not the exact imprint of the underlying deformation processes. Clearly, the observed waveform may have been affected by various other factors, such as the propagation and reflections of sound in the sample, the flatness of the transducer frequency band, etc. However, such extra-factors do not induce multifractal scaling, but rather obscure the scaling features arising from the plasticity mechanisms. Thus, although a thorough quantitative interpretation of individual AE hits on a short time scale may be rather involved, the above results suggest that the involved deformation processes display correlations giving rise to the multifractal character of the corresponding waveforms. Such multifractal features are often considered as a signature of cascade-like processes [79, 80].

4.4.2 Al-Mg polycrystals: multiscale analysis

The results presented in Sections 4.3 and 4.4.1 testified to the complex correlated behavior of deformation processes, respectively at the largest time scale corresponding to the duration of the mechanical test, and at the least time scale of individual AE events. However, these findings do not answer questions as to whether the self-organized nature of plastic deformation is manifested

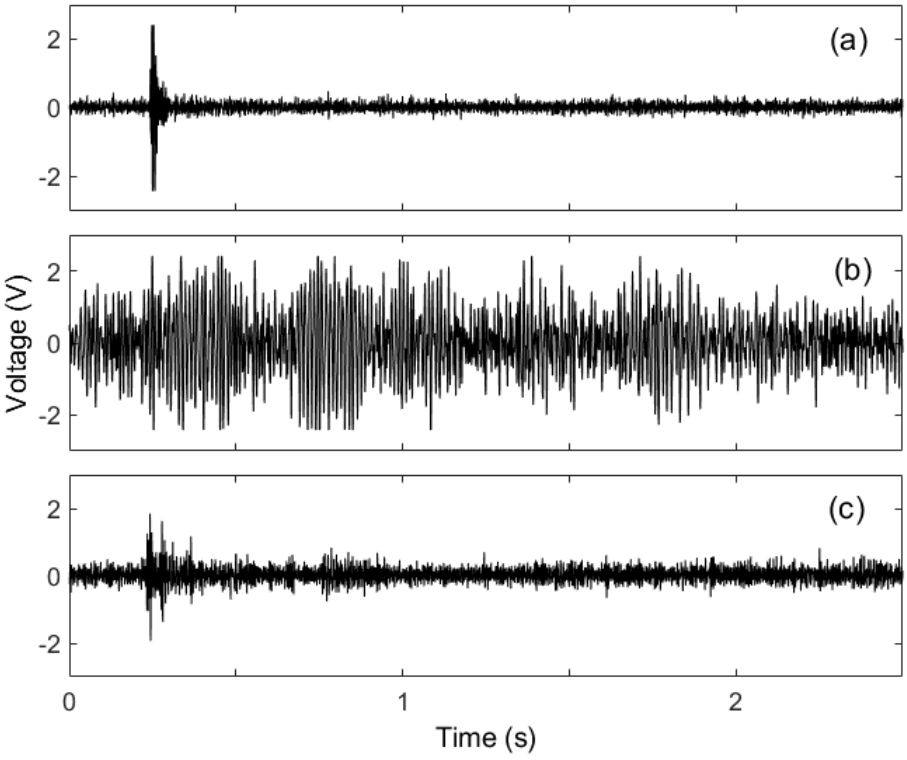

Figure 14: Examples of AE events observed at $\dot{\epsilon}_a = 2.9 \times 10^{-4} s^{-1}$. After [78], with permission of the Editor.

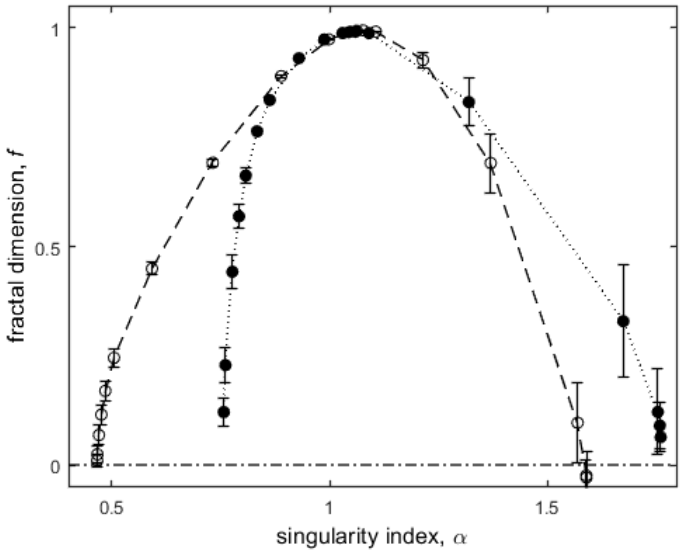

Figure 15: Singularity spectra $f(\alpha)$ for the AE signals shown in Fig. 14 (b) and (c): solid circles – Fig.14 (b); open circles – Fig. 14 (c). After [78], with permission of the Editor.

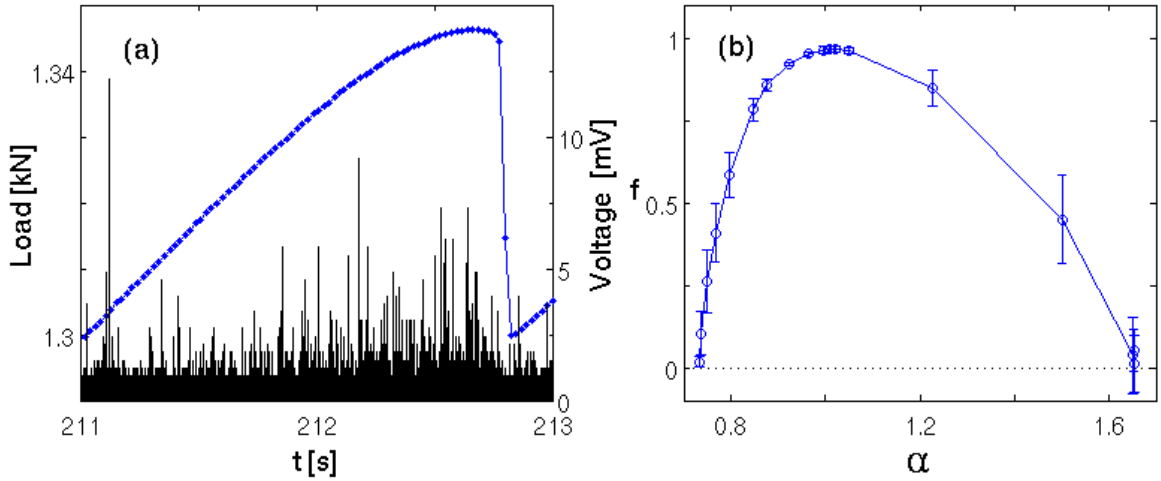

Figure 16: (a) Positive half-waves of the AE signal accompanying a reloading/serration sequence. (b) The corresponding singularity spectrum obtained after cutting off the part of the signal below $1.5mV$. After [83].

at all intermediate time scales, whether it corresponds to the same dynamics at the different scales, whether or not it involves the same mechanisms of spatial coupling and finally, whether the applied statistical methods provide a quantitative criterion allowing to distinguish between distinct underlying mechanisms. These questions are still awaiting meticulous investigations. Some of the first experimental efforts in this direction are presented below in the present section [81, 82, 83].

Tensile experiments were performed on polycrystalline samples with a $30 \times 7 \times 1\, mm^3$ gauge part, cut from a cold-rolled sheet of an $Al - 5\%Mg$ alloy. Part of the samples were solution-treated by annealing for $2\, h$ at $400°C$ and quenching in water. The grain size was about $4-6\, \mu m$ in the as-rolled conditions and twice as large after annealing. The samples were deformed at room temperature and a nominal strain rate $\dot{\epsilon}_a$ from $2 \times 10^{-5} s^{-1}$ to $6 \times 10^{-3} s^{-1}$. The AE was continuously recorded at a frequency of $2\, MHz$, using a piezoelectric sensor with a $200-900\, kHz$ frequency band. Records covering the entire test duration were realized at high enough strain rates: $\dot{\epsilon}_a \geq 2 \times 10^{-4} s^{-1}$. In slower tests, recording was performed at intervals up to 10 minutes, in order to get data-streamed files with a viable length. Finally, various approaches to signal denoising, namely wavelet procedures built in *Matlab* or signal truncation below a threshold, were applied to improve the detection of multifractal behavior (for more information on signal denoising, see, e.g., [44, 49, 84, 85, 86, 87]).

Using data streaming made it possible to confirm and refine the above results of the analysis of individual AE events in $Al - Cu$ alloy. AE events were observed not only during stress serrations but also during smooth plastic flow, both before the onset of the PLC effect and between stress drops. It was observed that the isolated decaying oscillations shown in Fig.14 (a) mainly occurred during reloading after deep stress drops of type B or C, *i.e.*, when the applied load was lower than the previously attained level and could not effectively activate dislocation motion. In addition, the data-streaming technique allowed extending the multifractal analysis to high strain rates, where the strong AE activity makes it difficult to extract individual events. The variety of waveforms detected by virtue of this technique included those illustrated in Fig.14, but also some additional characteristic shapes. Essentially, multifractal scaling similar to that reported in [78] was systematically found at short time scale, both in annealed and non-annealed conditions and at all strain rates.

Besides, smooth multifractal spectra were found at all strain rates when the length of the

analyzed interval was varied between its lower and upper bounds. However, the first data we have gathered suggest that the AE may not obey global scaling laws at low and medium strain rates. Fig.16 presents an example of multifractal analysis over an interval of $2\,s$ length covering a single reloading/serration sequence at $\dot{\epsilon}_a = 2 \times 10^{-4} s^{-1}$. The singularity spectrum was determined in a scaling interval $\delta t \approx [\,40ms; 0.6s\,]$. A similar spectrum was also found in a hundred-times longer interval covering many stress serrations, including the serration displayed in Fig. 16 (a). However, the lower limit of the corresponding scaling interval, $\delta t \approx [\,10s; 100s]$ does not embrace that for the single serration period. Moreover, multifractality was not found for time intervals covering a small number of stress serrations. These breaks in the scaling behavior became even more significant when the strain rate was reduced to the range corresponding to type C behavior. It was conjectured that they might be due to the strong intermittency of the AE activity at low strain rates, when periods of high activity are interlaced with long silent periods. This conjecture is in agreement with the trend to synchronization at slow loading rates mentioned in Section 4.3. However, it needs additional confirmation, as these breaks in scaling may also result from the signal denoising procedure, which could posibly remove a part of the useful signal together with its undesirable noisy part.

In contrast to the case of slow loading, multifractality was established for each choice of the time interval length at high strain rates. This result bears evidence to the formation of a globally correlated behavior, consistent with the SOC conjecture. However, the scaling indexes were found to vary with the size of the analyzed portion of the signal. In addition to the unavoidable influence of noise on the accurate determination of the scaling indexes, such variations may be due to the unsteadiness of the AE signal with deformation (which is of course also present at lower strain rates). Indeed, the quantitative analysis of the AE signals is complicated by the intrinsically non-stationary nature of the deformation process, which may also derail the search for universal scaling laws. Further evidence using various kinds of quantitative analysis will be needed in this case too.

As will become clear from the discussion of PLC effect modeling in the next section, the challenge for future investigations is most likely about the nature of spatial coupling in the heterogeneously deforming material. The observation of correlations over a wide range of time scales suggests the prevailing role of a coupling mechanism via internal stresses, which may involve both very short and very long characteristic time scales. The former kind derives from fast (and long-range) elastic reactions to local strain incompatibilities, the latter is due to the slow plastic relaxation of these incompatibilities, via microstructure rebuilding. Nevertheless, short-time/short-range correlations, which may play a significant role in cascade deformation processes, involve additional coupling mechanisms such as double cross-slip of screw dislocations [42], or direct shock-like triggering of dislocation breakaway by elastic waves.

5 Modeling approaches

Our early efforts to capture the salient statistical and dynamical properties of the PLC effect were based on a heuristic block-spring model [38, 39, 67, 88], in the spirit of stick-slip toy models applied at this time to interpret the Gutenberg-Richter law for earthquakes statistics [89, 90, 91]. The major conclusion of this work was that, jointly considering adequate nonlinear SRS of slip for each block and coupling between blocks through elastic springs allows for a qualitative prediction of the transitions between peaked and power-law statistics of stress serrations, as well as between static and propagating strain localization bands. The adopted coupling scheme reflected our feeling that internal stresses were likely candidates for spatial coupling in jerky flow. As indicated in the introduction section, our further modeling approaches of jerky flow were expected to provide answers to questions about the minimal spatial coupling mechanisms required to retrieve the complex spatio-temporal dynamics observed in both single and polycrystals, provided the local slip plane behavior was adequately modeled. The multifractal analyses had shown

that the long-range stresses and elastic waves associated with the presence of crystal defects and incompatibilities between differently strained regions were the prevailing spatial coupling mechanism, and that the short range interactions between dislocations arising during their transport in the material were also likely candidates. Hence, the above questions may be split as follows: in polycrystals, do the incompatibility stresses arising from differently strained regions induce sufficient spatial coupling to generate the various spatio-temporal patterns and dynamics pertaining to jerky flow, irrespective of the other potential sources of spatial coupling? In single crystals, are these other sources of coupling, *i.e.* the incompatibility stresses arising from the presence of dislocations and the short range interactions between dislocations, also sufficient to generate these various patterns and dynamics? Besides, is there a role of DSA in the modulation of this spatial coupling, and does the latter produce patterning and non trivial dynamics in its absence?

5.1 Polycrystals

5.1.1 Model

It is appropriate to use a polycrystal plasticity model embedded in a three-dimensional finite element framework to answer the above questions, since such a model is intrinsically consistent with the assumed origin of spatial coupling in polycrystals, *i.e.* the incompatibility stresses arising between differently strained regions. Let us denote by $\mathcal{I}$ the surface of discontinuity between two such regions D^- and D^+, possibly two neighbor grains, or a band of localized plastic strain and its weakly strained neighborhood. At any point on the interface $\mathcal{I}$, let $\mathbf{n}$ be the normal vector to the interface oriented from D^- to D^+. Continuity of matter and mechanical equilibrium across $\mathcal{I}$ respectively require that the displacement $\mathbf{u}$ and the traction vector $\mathbf{T}.\mathbf{n}$, where $\mathbf{T}$ is the stress tensor, be continuous across $\mathcal{I}$. Hence, if $[\![x]\!] = x^+ - x^-$ denotes the discontinuity in the variable x across $\mathcal{I}$, then $[\![\mathbf{u}]\!] = 0$ and $[\![\mathbf{T}.\mathbf{n}]\!] = 0$. The continuity of the traction vector is reflected as well by the continuity of the normal part, $\mathbf{T}_n = \mathbf{T}.\mathbf{n} \otimes \mathbf{n}$, of the stress tensor: $[\![\mathbf{T}_n]\!] = 0$, but the tangential part of $\mathbf{T}$, $\mathbf{T}_t = \mathbf{T} - \mathbf{T}_n$, may be discontinuous across the interface. Conversely, the continuity of the displacement at the interface requires tangential continuity of the total distortion tensor $\mathbf{U} = \mathbf{grad}\,\mathbf{u}$, or, in terms of the normal and tangential parts of the distortion, $\mathbf{U}_n = \mathbf{U}.\mathbf{n} \otimes \mathbf{n}$ and $\mathbf{U}_t = \mathbf{U} - \mathbf{U}_n$: $[\![\mathbf{U}_t]\!] = 0$. This tangential continuity condition is known as Hadamard's compatibility condition [92]. By requiring equality of terms on the left of the interface with terms on its right, both the equilibrium and compatibility conditions $[\![\mathbf{T}_n]\!] = 0$ and $[\![\mathbf{U}_t]\!] = 0$ introduce non locality in the model. Both are intrinsically satisfied by finite element modeling of the polycrystal. The discontinuities of $\mathbf{T}_t$ and $\mathbf{U}_n$ naturally induce incompatibility stresses across $\mathcal{I}$. No other spatial coupling factor is additionally introduced in the model.

Only the main features of the formulation of the constitutive model are presented in the following. Further details, as well as the finite element implementation and the solution methods are available in [40]. Consider first the kinematics and material behavior of single crystals. Since elastic unloading of the sample is resulting from localized plastic events, elasto-plastic constitutive laws are needed. Regarding elasticity, linearity and isotropy are simply assumed. The plastic velocity gradient tensor $\mathbf{L}_p$ derives from the linear combination of the Schmid tensors on all slip systems, *i.e.* of the dyadic products of $\mathbf{b}_s$ and $\mathbf{n}_s$, respectively the unit vectors along the slip direction and the direction normal to the slip plane (s):

$$\mathbf{L}_p = \sum_s \dot{\gamma}_s \mathbf{b}_s \otimes \mathbf{n}_s. \tag{10}$$

Here, $\dot{\gamma}_s$ denotes the plastic shear rate on slip system (s). The Schmid resolved shear stress τ_s on slip system (s) is obtained from the projection of the crystal stress tensor $\mathbf{T}_c$ on this

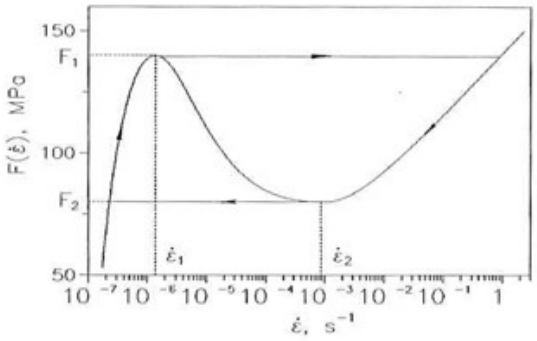

Figure 17: Nonlinear strain rate dependence of the flow stress in the presence of DSA. In the intermediate strain rate range $\dot{\epsilon}_1 < \dot{\epsilon} < \dot{\epsilon}_2$, the SRS is negative and a uniform plastic flow is unstable. When the applied strain rate $\dot{\epsilon}_a$ falls in this range, the models in [35, 36, 40] predict an instantaneous forward jump of the local strain rate to the positive SRS range at high strain rates, corresponding to dislocation unpinning at critical point $(\dot{\epsilon}_1, F_1)$, followed by an instantaneous jump backward at the critical point $(\dot{\epsilon}_2, F_2)$, corresponding to dislocation re-pinning. After [39], with permission of the Editor.

tensor: $\tau_s = \mathbf{b}_s \otimes \mathbf{n}_s : \mathbf{T}_c$[1], and is related to the slip system plastic shear rate $\dot{\gamma}_s$ through the non-Newtonian viscoplastic power law

$$\dot{\gamma}_s = \dot{\gamma}_0 |\frac{\tau_s}{\tau_0}|^n sgn(\tau_s), \tag{11}$$

which ensures uniqueness of the slip activity on all slip systems, with the SRS parameter $n = 20$. Such a large n value reflects the abruptness of dislocation unpinning. The constitutive behavior also derives from the choice of the reference strain rate $\dot{\gamma}_0$ and stress τ_0. Assuming isotropy of hardening, $\dot{\gamma}_0$ is chosen to be the current local equivalent strain rate, whereas τ_0 is the current glide resistance on a slip system. Based on the model [36] for DSA, it is written as:

$$\tau_0 = \tau_a + \tau_h + S_0 ln(\dot{\gamma}_0) + f(1 - exp(-(\frac{\dot{\gamma}^*}{\dot{\gamma}_0})^{2/3})), \tag{12}$$

where τ_a is an athermal stress characterizing the rate independent interactions of dislocations with long-range obstacles, while τ_h represents strain hardening and dynamic recovery effects, via a modified Voce law [40]. S_0 is the SRS of the flow stress associated with the thermal activation of short-range obstacles overcoming in the absence of DSA. f is the saturation level of the solute pinning stress and $\dot{\gamma}^*$ is a strain rate characterizing solute diffusion at constant temperature. All material parameters were chosen to fit the behavior of the $Al-2.5\%Mg$ alloy used in the experiments in [63]. Plastic relaxation occurs through the combined effect of short-range obstacles overcoming and dynamic recovery. It can be characterized by the time scale $t_R = \tau_0/\mu \sum_s |\dot{\gamma}_s|$, which can be seen as the ratio of the effective viscosity $\tau_0/\sum_s |\dot{\gamma}_s|$ to the elastic modulus μ. From Eq.12, the aging properties of dislocations involve three ranges of shear rates $\dot{\gamma}_0$, with different SRS signs, as illustrated in Fig.17. At sufficiently low strain rates, the dislocations are pinned on their obstacles, and the flow stress increases with strain rate (positive SRS). At sufficiently large strain rates, the dislocations are unpinned, with again a positive SRS. If the local strain rate $\dot{\gamma}_0$ falls into the intermediate range of negative SRS, the flow stress τ_0 decreases as the strain rate increases. The local state $(\tau_0, \dot{\gamma}_0)$ is therefore unstable and cannot be sustained on a slow time scale. When the stress and local strain rate increase in the low strain rate domain, the dislocations finally end up overcoming the unpinning critical threshold stress and, by algorithmic

[1]The (double) dot product of two tensors denotes the contraction of these tensors with respect to the last index (two indices) of the first one and the first index (two indices) of the second one.

rule, instantly jump at constant stress to the high strain rate domain of positive SRS, where the system is overdriven. Thus, Eq.12 is complemented by the constraint that the local plastic strain rate $\dot{\gamma}_0$ may not take values in the range of instability. When the applied strain rate $\dot{\gamma}_a$ is chosen in this range, the strain rate field is necessarily inhomogeneous, with local strain rates distributed either in the low strain rate domain or in the high strain rate domain, both with positive SRS. A similar algorithmic rule applies at unloading from the overdriven state. With decreasing stress and local strain rate in the high strain rate domain of positive SRS, the dislocations become abruptly arrested again on obstacles and the local strain rate instantly overshoots back to the low strain rate domain of positive SRS, without transiting through the forbidden range of negative SRS. Eventually, the cycle arrest/breakaway keeps on repeating as the stress keeps on increasing. From the supplementary involvement of an algorithmic rule, it is apparent that Eqs.(11,12) do not fully describe the local behavior of the material. Only slow variations are considered, and fast variations, *i.e.* those occurring at the time scale of the arrest-breakaway cycle, approximately the time scale t_L for reloading between stress drops, are actually accounted for through instantaneous jumps. A fully dynamical description was obtained by introducing in particular a new independent variable, that is subject to variations on a fast time scale, namely the aging time t_a of dislocations on their obstacles [37], as will be recalled below in Section 5.2.1.

As for the polycrystalline behavior, each Gauss point of the finite element mesh was assigned a polycrystal comprising N grains, all deforming with the same velocity gradient tensor $\mathbf{L}$. Typically $N = 8$, which leads, with the finite element mesh usually employed (1440 brick elements in a $5 \times 8 \times 36$ arrangement), to 92160 grains in the sample. The stress tensor $\mathbf{T}$ at Gauss points is obtained from the average of all the crystal stress tensors $\mathbf{T}_c$ at this point, *i.e.* $\mathbf{T} = \frac{1}{N} \sum_{c=1}^{N} \mathbf{T}_c$. Thus, the material behavior at Gauss point P derives from the combined material responses of N grains in a representative volume surrounding P. From different grain states, such as those arising from different initial crystallographic orientations, different crystal stress tensors $\mathbf{T}_c$ may emerge, but only the averaged tensor $\mathbf{T}$ of the aggregate does satisfy mechanical equilibrium and the boundary conditions. Velocity boundary conditions were imposed at the sample ends. Free rotation of the moving end was allowed, while rigid body rotation of the clamped end was prevented by using minimal displacement constraints.

5.1.2 Results

- High strain rates

  At the high applied strain rate $\dot{\epsilon}_a = 10^{-3} s^{-1}$, close to the upper limit of the range of negative SRS, the model unambiguously shows continuous band propagation (see Fig.18), consistent with the observations of type A bands in this range of strain rates. As the next item will show, continuous propagation disappears upon decreasing the driving velocity. Hence, band propagation stems from the properties of spatial coupling in this range. The statistical analysis of the computed stress time series show in addition that the stress drop size and duration distributions scale according to the power laws $p(\Delta\sigma) \propto \Delta\sigma^{-\alpha}$, $p(\Delta t) \propto \Delta t^{-\beta}$ with $\alpha = 1.35$ and $\beta = 1.92$. Further, $\Delta\sigma$ also scales as δt^h with $h = 2.85$. The three exponents (α, β, h) satisfy the consistency relation $\beta = 1 + h(\alpha - 1)$, which confirms the scaling behavior of the stress drops. Such behavior is consistent with the evidence of power laws in the distributions of stress rate bursts and durations in experimental signals from polycrystalline $Al - 2.5\%Mg$ samples at strain rate $\dot{\epsilon}_a = 1.39 \times 10^{-3} s^{-1}$ [63], as recalled in Section 4.2.2. Thus, both the experimental and predicted stress drop distributions are consistent with SOC dynamics, and suggest the presence of strong spatial correlations at high strain rates.

- Low strain rates

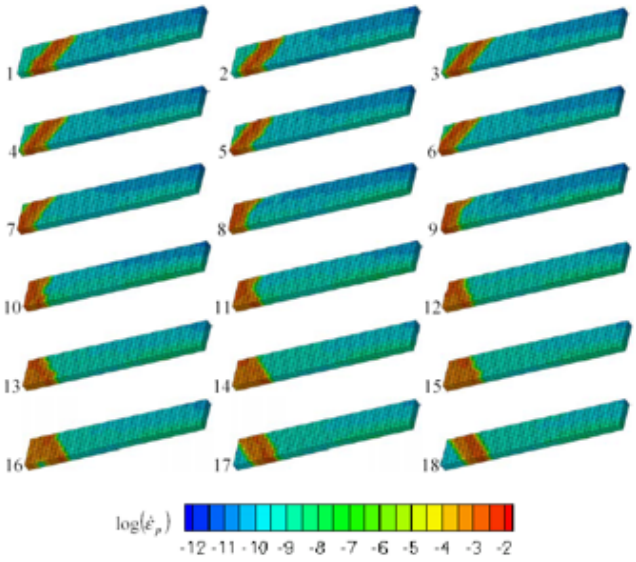

Figure 18: Strain rate contours of type A propagating bands at the applied strain rate $\dot{\epsilon}_a = 10^{-3}s^{-1}$ in $Al - Mg$ simulated polycrystal. The sequence is taken from a simulation with eight grains per Gauss point. It shows a band bouncing off the left end of the sample, an event accompanied by a large stress drop. The time increment between consecutive images is $0.05s$, strongly suggesting continuous propagation. Note that the band changes orientation after bouncing off. After [40], with permission of the Editor.

Recall that serrations closely approaching the behavior of type C bands were observed at low applied strain rates in the cold-rolled $Al - 2.5\%Mg$ polycrystalline alloy not subsequently annealed (see Section 4.2.2 and reference [63]). A similar microstructure was simulated by imposing a rolling texture to the sample, with the rolling and normal directions aligned with its largest and shortest dimensions, respectively. The simulation of a tension test at the applied strain rate $\dot{\epsilon}_a = 5\times10^{-5}s^{-1}$ then revealed a series of static bands nucleating at random locations along the sample, and having irregular appearance and orientation as illustrated in Fig.19, consistent with type C bands experimentally observed in this range of strain rates [63]. Further, the simulated stress time series were strikingly different from the curves associated with type A shown above. The distributions $p(\Delta\sigma)$ and $p(\Delta t)$ for the stress drop size $\Delta\sigma$ and duration Δt had a peaked character, as was also observed in the data from experimental time series at low strain rates. Thus, despite the presumably high level of spatial correlations induced by the initial uniform texture imposed to the material, neither band propagation nor spatial correlations between successive bands occurred. In order to explain that dramatic shift in the dynamics, the time scale t_R for the plastic relaxation of the internal stresses was computed, and found to be $t_R \approx 0.05\,s$, much shorter than the average reloading time $t_L \approx 2s$ between successive stress drops. Therefore, relaxation of the internal stresses occurs before the next band nucleates, which dramatically weakens the spatial correlations between consecutive bands. Thus, the notion that the static and uncorrelated character of type C bands is due to plastic relaxation of internal stresses during reloading between serrations when $t_R \ll t_L$ is supported by the simulation. Enrichment of this conjecture through synchronization of small scale plastic events will come later in eventual research, and will be discussed below in Section 6.

- Medium strain rates

  In tensile tests simulated at strain rate $2 \times 10^{-4}s^{-1}$ in the mid-range of strain rates, successive bands were found along the sample. Each band was static, but newly nucleated

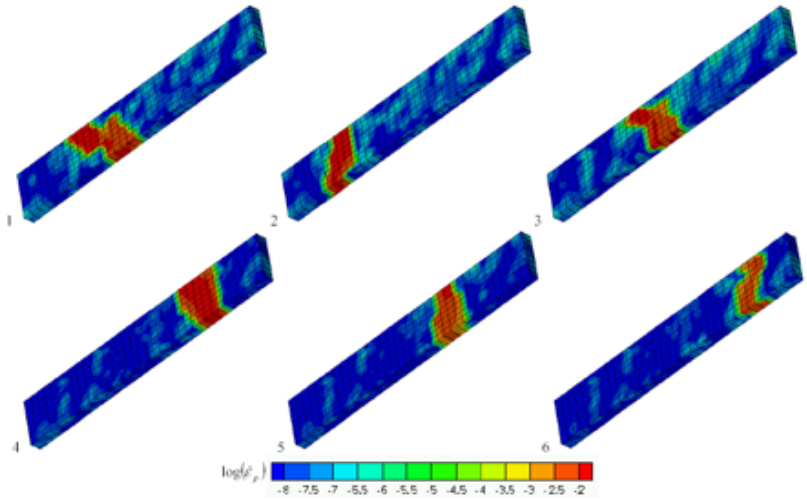

Figure 19: Strain rate contours of Type C static bands obtained for an applied strain rate $\dot{\epsilon}_a = 5 \times 10^{-5} s^{-1}$ in $Al - Mg$ simulated polycrystal. Note that bands occur and are oriented randomly along the sample. After [40], with permission of the Editor.

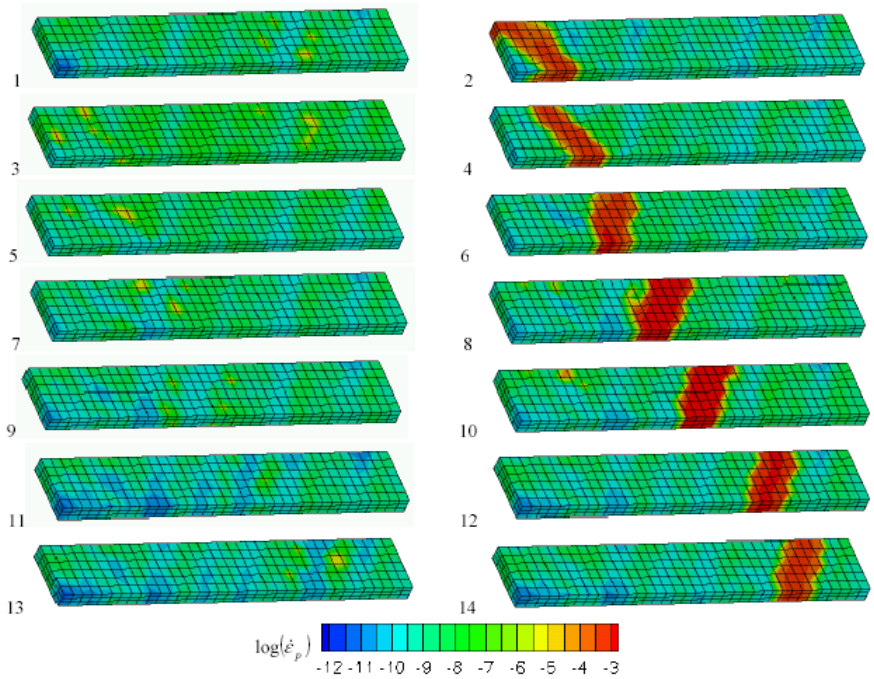

Figure 20: Strain rate contours of Type B hopping bands obtained for an applied strain rate $\dot{\epsilon}_a = 2 \times 10^{-4} s^{-1}$ in $Al - Mg$ simulated polycrystal. Right: location of successive bands. Left: intermediate images showing local strain rate increases prior to band nucleation, followed by local decreases upon band disappearance. After [40], with permission of the Editor.

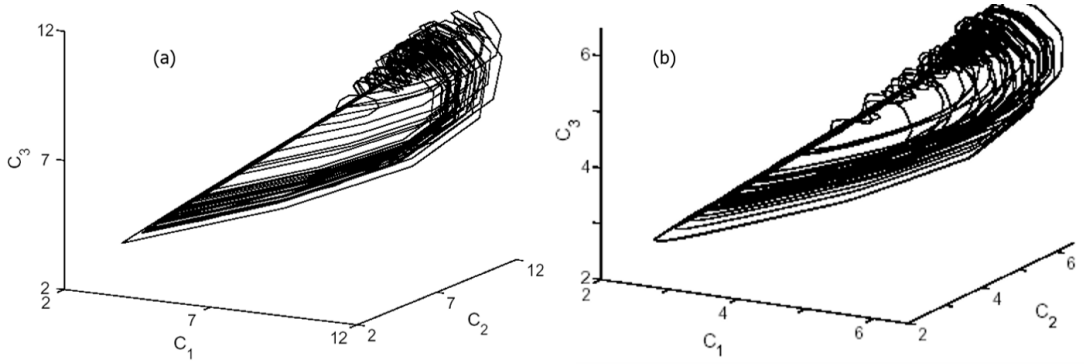

Figure 21: Strange attractors from experiment (a) and model (b) in the $3-D$ subspace of the reconstructed phase space associated with the first three principal values of the trajectory matrix, in $Al-Mg$ simulated polycrystal and $Al-2.5\%Mg$ polycrystal at strain rate $\dot{\epsilon}_a = 2\times10^{-4}s^{-1}$ corresponding to Type B bands. The quasi-straight parts correspond to reloading sequences, the curved ones to plastic events. After [40, 63], with permission of the Editor.

bands formed ahead of the previous ones, giving the visual impression of a propagating plastic front (see Fig.20). The statistical analysis of the predicted stress time series indicated that the distributions $p(\Delta\sigma)$ and $p(\Delta t)$ for the stress drop size $\Delta\sigma$ and duration Δt had complex asymmetric shapes with one or several peaks indicating the presence of characteristic scales. These are features expected from the type B bands commonly observed in polycrystals at medium applied strain rates. Note that the plastic relaxation time scale t_R was found to increase with the plastic strain rate, while the reloading time scale t_L decreased. This trend resulted in t_R being of the order of t_L at this strain rate. Deterministic chaos was found, first by computing the correlation dimension and Lyapunov spectrum. A scaling region was obtained for the correlation function, of which the slopes converged to $\nu \approx 4.26$ as the embedding dimension approached $d = 16$, which reflects self-similarity of the reconstructed attractor. The Lyapunov spectrum was calculated for the embedding dimension $d = 6$. Positive and zero exponents were found, with stable values when the size of the shell used to sample the data points was varied. Further, the consistency check based on the calculation of the Lyapunov dimension D_{KY} turned out to give $D_{KY} \approx 4.5$. Similar dynamic features were reported in reference [63] and Section 4.2.2 for the experimental stress time series associated with type B bands in $Al-2.5\%Mg$ polycrystals, which led to $\nu \approx 4.15$ and $D_{KY} \approx 4.2$. This excellent agreement between simulated and experimental values indicates that the model can reproduce the spatio-temporal behavior of type B bands, as well as involved details of their dynamics. Another example of this ability is provided by plots of the reconstructed attractor in a three-dimensional subspace of the reconstructed phase space, for both the predicted and experimental stress time series. The plots, shown in Fig.21, obtained after singular value decomposition of the trajectory matrix and restriction to its first three largest principal values, are indeed strikingly similar. Thus, both the experimental and simulated results are consistent with the existence of a chaotic regime in this range of applied strain rates.

5.1.3 Discussion

From the results recalled above, it appeared clearly that considering spatial coupling as being due to strain incompatibilities was sufficient to account for the sequence of band types and dynamic properties of jerky flow, despite the absence of both short range and long range interactions between dislocations. It was also realized that a comprehensive description of this sequence of regimes called for multiscale connections between the basic ingredients of the model, namely DSA at slip plane level, rate dependent polycrystal plasticity at mesoscale and the finite element

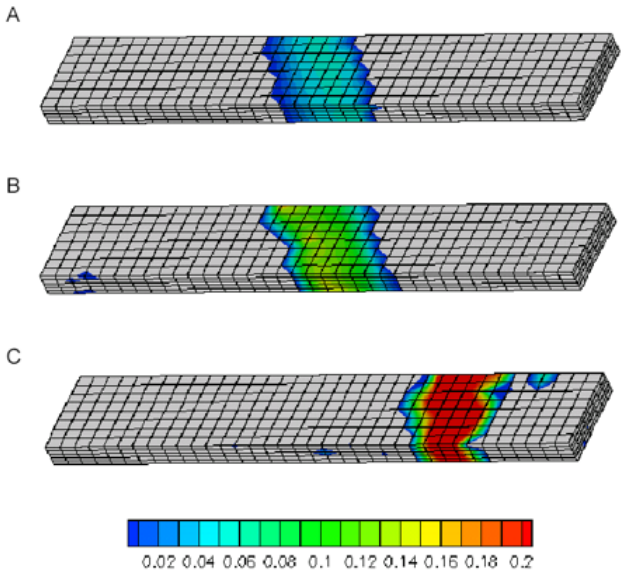

Figure 22: $Al - Mg$ simulated polycrystal : distribution over the sample of the plastic strain rate offset from its critical threshold value (*i.e.* the lower limit of the negative SRS range). (A) SOC dynamics, (B) chaotic dynamics, (C) quasi-random regime. Note that all plastic strain rates remain close to their critical value in SOC dynamics (Hence, the words "Self Organized Criticality"). Offsets from the threshold are larger in the chaotic dynamics and even larger in the quasi-random regime. After [40], with permission of the Editor.

framework for the numerical solution of the boundary value problem at macroscale.

The comparison of time scales is indeed fundamental to understanding the PLC effect. In the first place, jerky flow occurs only when the characteristic time for solute diffusion at dislocation scale $\tau^* = 1/\dot{\gamma}^*$ is of the order of the macroscopic loading time scale $1/\dot{\gamma}_a$. Indeed, if $\tau^*\dot{\gamma}_a \ll 1$, dislocation obstacles are constantly fully saturated with solute atoms. If conversely $\tau^*\dot{\gamma}_a \gg 1$, dislocation aging cannot even take place. In both cases, repeated dislocation pinning-unpinning sequences cannot occur. Between these extreme situations, when $\tau^*\dot{\gamma}_a \approx 1$, the strength of obstacles to dislocation motion increases if $\tau^*\dot{\gamma}_a$ decreases. The serrations size is in line with the strength of the obstacles. It increases from type A to type C serrations, as can be noticed in Fig.1, when the product $\tau^*\dot{\gamma}_a$ decreases. Indeed, the waiting time of dislocations arrested at their obstacles increases as $\dot{\gamma}_a$ decreases at constant τ^*, which offers more time for aging and leads to stronger obstacles. Conversely, decreasing τ^* at constant strain rate $\dot{\gamma}_a$ favors solute diffusion toward obstacles, which also leads to stronger obstacles. In both cases the product $\tau^*\dot{\gamma}_a$ decreases. An increase of the diffusivity in a single test at constant strain rate $\dot{\gamma}_a$, *i.e.* a decrease of τ^* (and hence of $\tau^*\dot{\gamma}_a$) with strain, may also play a leading role in the occurrence of a critical strain ϵ_{cr} for instability (see [93] and references therein).

In a similar way, and as suggested in Section 5.1.2, it is revealing to compare the characteristic relaxation time scale t_R, which arises from mesoscale phenomena, with the reloading time scale t_L, which derives from the imposed boundary conditions at macroscale. At high strain rates, little time is allowed for the relaxation of incompatibility stresses between reloading events since $t_R \gg t_L$, and a high degree of spatial correlation therefore exists. A spatially uniform plastic strain rate field is "close" to satisfying the boundary value problem. Most local plastic strain rates stay close to the threshold value for localized plastic events, as illustrated in Fig.22. As a consequence, the latter can occur on any scale, although in a limited range of not too large scales, which leads to scaling stress drop distributions and therefore to SOC-type behavior in this range. As the applied strain rate is decreased in the medium strain rate range, the plastic

relaxation time t_R becomes of the order of the reloading time t_L ($t_R \approx t_L$). Thus, partial plastic relaxation of incompatibility stresses occurs, but spatial coupling is still marginally efficient. The correlation distance is still large enough to induce the hopping bands associated with chaotic dynamics. The system is increasingly overdriven, meaning that a large dislocation subset remains in the pinned state. Therefore, accommodation of the imposed strain rate can only be achieved through relatively large localized plastic offsets from the critical threshold of instability, *i.e.* through collective dislocation breakaways from sufficiently strong obstacles. As the applied strain rate is further decreased, the incompatibility stresses become almost fully relaxed because the plastic relaxation time becomes much shorter than the reloading time ($t_R \ll t_L$), and spatial coupling all but vanishes, which induces static bands, randomly distributed over the sample and displaying a large span of plastic bursts originating in dislocation breakaways from strong obstacles to dislocation motion. Remarkably, the sequence of dynamic regimes within the range of PLC effect is therefore governed by the competition of the time scales (t_L, t_R), and conditioned by the value of the product $\tau^*\dot{\gamma}_a$. Thus, the wealth of dynamic behavior displayed by the PLC effect results from the various combinations offered by the material nonlinearity at slip plane level and the spatial correlations at mesoscale, when the applied strain rate is varied at sample scale. As shown in Section 4.3 by AE monitoring of jerky flow in polycrystals, the synchronization of small scale events plays a significant role in building large plastic events, particularly at low strain rates. As mentioned above in Section 5.1.2 and thoroughly discussed below in Section 6, involving in the discussion the synchronization process and its evolution with the driving rate will further substantiate and add complexity to the present interpretation.

5.2 Single crystals

Recall that the situations of interest comprise both the spatio-temporal dynamics of the plastic events occurring in the presence of DSA, and the dynamics of small scale plastic events, which also occur in the absence of DSA. Since the model developed above in Section 5.1.1 assigns spatial coupling, although partly, to grain-to-grain incompatibility stresses, it is clearly unfit for single crystals. In such circumstances, the boundary value problem may instead be addressed through the finite element discretization of the mechanics of dislocation fields [41]. In addition to static equilibrium and continuity of matter, spatial coupling then derives from the long-range stresses associated with the presence of dislocations and from the short-range interactions encountered by dislocation in their motion through the material [94, 95, 96]. Long-range incompatibility stresses are unavoidable in the presence of dislocations. Short-range interactions between dislocations such as dislocations junctions, line length increase from dislocation sources, climb of edge dislocation or double cross-slip of screw dislocations, are all reflected at the resolution length scale of dislocation densities by their transport through the material. Both lattice incompatibility and dislocation transport are fully ingrained in plasticity, which is therefore seen in this model as an inherently spatially correlated phenomenon.

5.2.1 Model

The model uses dislocation densities as state variables, at a resolution length scale smaller than the scale employed for the macroscopic variables in the more conventional model of Section 5.1.1. Dislocations have been classified into excess or polar dislocations, or Geometrically Necessary Dislocations (GNDs), and statistically distributed dislocations, or Statistically Stored Dislocations (SSDs). These concepts are scale-dependent, since all dislocations are excess dislocations at a sufficiently small scale of resolution. However, once a scale is chosen, statistically distributed dislocations contribute only to the overall plastic flow and not to lattice incompatibility, unlike excess dislocations, which contribute to both. Excess dislocations, their long-range stresses and their transport, were modeled using the mechanics of dislocation fields, and statistically distributed dislocations using crystal plasticity with or without DSA.

- Mechanics of dislocation fields
  The characterization of excess dislocations employs the continuum description of lattice incompatibility based upon Nye's dislocation density tensor $\boldsymbol{\alpha}$. Operating on the normal $\mathbf{n}$ to a unit surface S, $\boldsymbol{\alpha}$ provides the net Burgers vector $\mathbf{b} = \boldsymbol{\alpha}.\mathbf{n}$ of all dislocation lines threading S, *i.e.* the incompatibility in elastic displacement found along the Burgers circuit surrounding this surface. Because of this incompatibility, the elastic distortion (strain and rotation) tensor $\mathbf{U}_e$ is not a gradient. It has an incompatible part, $\mathbf{U}_e^{\perp}$, which results from the distribution $\boldsymbol{\alpha}$ and is the gradient-free solution to the incompatibility equation

$$\mathbf{curl}\,\mathbf{U}_e^{\perp} = \boldsymbol{\alpha} \tag{13}$$

  written here at small strains[2]. Its compatible part, $\mathbf{U}_e^{\parallel}$, is a gradient. For small strains, it is the difference between the displacement gradient $\mathbf{U} = \mathbf{grad}\,\mathbf{u}$ and the compatible part of the plastic distortion, $\mathbf{U}_p^{\parallel}$: $\mathbf{U}_e^{\parallel} = \mathbf{U} - \mathbf{U}_p^{\parallel}$. At the resolution length scale used here (the characteristic size of unit surface S), the total plastic distortion rate $\dot{\mathbf{U}}_p$ results from the motion of the excess dislocations $\boldsymbol{\alpha}$, with (averaged over S) velocity $\mathbf{V}$, and of the (mobile) statistically distributed dislocations through the conventional plastic velocity gradient tensor $\mathbf{L}_p$ [3]:

$$\dot{\mathbf{U}}_p = \boldsymbol{\alpha} \times \mathbf{V} + \mathbf{L}_p. \tag{14}$$

  The incompatible part, $\dot{\mathbf{U}}_p^{\perp}$, of $\dot{\mathbf{U}}_p$ feeds the increments of excess dislocations through the transport equation for dislocation densities:

$$\mathbf{curl}\,\dot{\mathbf{U}}_p = -\dot{\boldsymbol{\alpha}}, \tag{15}$$

  which also reads, using Eq.14:

$$\dot{\boldsymbol{\alpha}} + \mathbf{curl}\,(\boldsymbol{\alpha} \times \mathbf{V} + \mathbf{L}_p) = 0. \tag{16}$$

  As indicated above, Eq.16 reflects the motion of individual dislocations and their short range interactions with neighboring dislocations at the resolution length scale of dislocation densities. Being a hyperbolic equation, it describes the excess dislocation densities as propagating along real characteristic lines through the material. High resolution DIC experiments in Cu single crystals confirmed the presence of such a propagation, with a velocity with respect to the material of the order of $10^{-2}\,m.s^{-1}$ at moderate strains [42]. The stress tensor $\mathbf{T}$ is obtained from the fourth order tensor of elastic constants $\mathbf{C}_e$ as the product

$$\begin{aligned} \mathbf{T} &= \mathbf{C}_e : \{\mathbf{U}_e\} = \mathbf{C}_e : \{\mathbf{U}_e^{\parallel} + \mathbf{U}_e^{\perp}\} \\ &= \mathbf{C}_e\{\mathbf{U} - \mathbf{U}_p^{\parallel} + \mathbf{U}_e^{\perp}\} \end{aligned} \tag{17}$$

  where $\{\mathbf{A}\}$ denotes the symmetric part of tensor $\mathbf{A}$. In this relation, $\mathbf{U}_e^{\perp}$ is obtained from the solution of Eq.13, and the integration in time of the compatible part, $\dot{\mathbf{U}}_p^{\parallel}$, of the plastic distortion rate $\dot{\mathbf{U}}_p$ provides the compatible plastic distortion tensor $\mathbf{U}_p^{\parallel}$. Note that $\mathbf{T}^{\perp} = \mathbf{C}_e : \{\mathbf{U}_e^{\perp}\}$ is the tensor of incompatibility (or internal) stresses. Its complement $\mathbf{T}^{\parallel} = \mathbf{C}_e : \{\mathbf{U}_e^{\parallel}\}$ allows the stress tensor $\mathbf{T} = \mathbf{T}^{\perp} + \mathbf{T}^{\parallel}$ to satisfy the equilibrium equation

$$\mathbf{div}\,\mathbf{T} = 0 \tag{18}$$

  and the boundary conditions. Finally, in order to close the model, constitutive relations are needed for the evolution of the statistical dislocation densities involved in the velocity

[2] In an orthogonal basis of unit vectors, the components of the curl of second order tensor $\mathbf{A}$ are $(\mathbf{curl}\,\mathbf{A})_{ij} = e_{jkl}A_{il,k}$, with summation on the repeated indices. The components e_{jkl} of the alternating tensor $\mathbf{X}$ are $e_{jkl} = \pm 1$ depending on whether the permutation of (j,k,l) is even or uneven, and $e_{jkl} = 0$ otherwise.

[3] In an orthogonal basis of unit vectors, the components of the vectorial product $\mathbf{A}\times\mathbf{V}$ between the second-order tensor $\mathbf{A}$ and the vector $\mathbf{V}$ are $(\mathbf{A} \times \mathbf{V})_{ij} = e_{jkl}\mathbf{A}_{ik}\mathbf{V}_l$, with summation on the repeated indices.

gradient $\mathbf{L}_p$ (see next item below), and for the (averaged) velocity $\mathbf{V}$ of the excess dislocations. The simplest possible constitutive relations for the latter are obtained in alloys at relatively high temperature, when climb of edge dislocations is possible and plasticity is therefore pressure-dependent. Then, the (averaged) dislocation velocity $\mathbf{V}$ is aligned with the driving force $\mathbf{F}$ on excess dislocations, *i.e.* the averaged Peach-Koehler force on a dislocation ensemble, according to:

$$\begin{aligned} \mathbf{F} &= \mathbf{T}.\boldsymbol{\alpha} : \mathbf{X} = B\mathbf{V}, \\ F_i &= e_{ijk}T_{jr}\alpha_{rk} = BV_i, \end{aligned} \tag{19}$$

where B is a positive viscous drag parameter ensuring positiveness of the mechanical dissipation. If the dislocation density tensor is written as $\boldsymbol{\alpha} = \mathbf{b} \otimes \mathbf{t}$, $\alpha_{rk} = b_r t_k$, where $\mathbf{b}$ is the Burgers vector and $\mathbf{t}$ the line vector for a dislocation subset threading normally an elementary surface, Eq.19 can also be written as

$$\mathbf{F} = \mathbf{T}.\mathbf{b} \times \mathbf{t} = B\mathbf{V}, \tag{20}$$

where the driving force is reminiscent of the true Peach-Koehler force on a single dislocation. When climb of edges is impossible, plasticity is independent of pressure and the constitutive relations become slightly more involved, as angular deviations between the (averaged) driving force and (averaged) dislocation velocity then take place [96]. Complemented with Eq.19 and the constitutive relations for SSDs below, Eqs.(13-18) form a complete set of equations, in the sense that it contains enough statements to derive uniquely the unknown displacement, stress and (GND, SSD) density fields, in a bounded domain from boundary and initial conditions. Boundary conditions comprise the conventional stress and displacement conditions, and possibly the specification of inward fluxes of dislocations.

- Crystal plasticity with/without Dynamic Strain Aging

The crystal plasticity formalism was reformulated in terms of SSD densities, namely the forest density ρ_f and mobile density ρ_m, the SSD velocities v_s per slip system and the aging time t_a, all subject to variations on both the (comparatively) slow time scale of the experiment and the fast time scale of the strain rate bursts. Hence, in the presence of DSA, Eqs.(10,11,12) become

$$\mathbf{L}_p = \sum_s \rho_m b v_s \mathbf{b}_s \otimes \mathbf{n}_s, \tag{21}$$

$$v_s = v_0 sgn(\tau_s) exp(\frac{|\tau_s| - \tau_a - \tau_h - \tau_{sp}}{\tau_0}), \tag{22}$$

where b is the Burgers vector magnitude and v_0 a reference velocity. $\tau_h = \alpha\mu b\sqrt{\rho_f}$ represents the conventional Taylor hardening (α being a constant and μ the shear modulus) and τ_{sp} is the solute-pinning stress

$$\tau_{sp} = f(1 - exp(-(\frac{t_a}{\tau^*})^{2/3})), \tag{23}$$

with $\tau^* = 1/\dot{\gamma}^*$ as the characteristic time for solute diffusion. Following [37], three Ordinary Differential Equations (ODEs) were specified for the coupled evolution of the mobile and forest densities (ρ_m, ρ_f) and aging time t_a. In this system of ODEs, multiplication of dislocations by loop generation, mutual annihilation leading to creation of dipoles and debris, immobilization of mobile dislocations through interactions with forest dislocations are represented, as well as dynamic recovery. Coupling between statistically distributed and excess dislocations occurs through the contribution of excess dislocations to the forest density, and also, the other way around, through Eq.16: the incompatible part of the

plastic velocity "gradient", $\mathbf{L}_p^{\perp}$, acts as a source term and generates excess dislocations. In addition, terms accounting for DSA govern the exchanges between ρ_m and ρ_f occurring during the arrest of dislocations by solute atoms, through a probability for dislocation arrest. Introducing this system of ODEs renders obsolete the algorithmic switches used in [40] to rule out the access of dislocations to the "forbidden" negative SRS domain. The price to pay for a better rendering of the phenomenon on short time scales is the increased numerical complexity of the computer code, which must be designed to account simultaneously for evolutions of the dislocation densities on a slow time scale in most parts of the sample and their stiff evolutions on a fast time scale in the regions where the plastic activity localizes.

In the absence of DSA, the crystal plasticity formalism becomes obviously much simpler. Eq.22 becomes

$$v_s = v_0 sgn(\tau_s) exp(\frac{|\tau_s| - \tau_a - \tau_h}{\tau_0}). \tag{24}$$

Alternatively, the power law

$$v_s = v_0 sgn(\tau_s)(\frac{|\tau_s|}{\tau_a + \tau_h})^n, \tag{25}$$

with the rate-sensitivity parameter $n = 20$, may be used to describe weak rate sensitivity of the shear stress. Eq.21 remains unchanged, while Eq.23 disappears. Therefore, only two ODEs are needed to govern the evolution of the mobile and forest SSD densities (ρ_m, ρ_f), in which, clearly, the terms accounting for dislocation arrest by solute atoms do not play a part anymore.

5.2.2 Results

Results from numerical simulations based on the above model and carried out in [41, 42] are now presented, in alloyed single crystals featuring DSA and in pure metals or in ice.

- Single crystal with Dynamic Strain Aging

  In [41], the single crystal sample of dimensions $2\,mm \times 0.5\,mm \times 12\,mm$ was oriented for single-slip, with the crystal direction $< 134 >$ coinciding with the tensile axis. The material properties were representative of an $Al - Mg$ alloy. The finite element mesh used 14400 brick elements in a $12 \times 6 \times 200$ arrangement. The refinement was such that bands were resolved by a few elements (about 8 elements across), allowing a study of their internal structure. The fixed end of the tensile sample was clamped, *i.e.* all velocity degrees of freedom were constrained, while the other end was subjected to constant velocity in the axial direction. There was no initial heterogeneity introduced in either material properties or initial conditions.

  After the initial elastic loading, the simulation of a tensile test at the applied strain rate $\dot{\epsilon}_a = 5 \times 10^{-5} s^{-1}$ exhibited the Lüders phenomenon, *i.e.* an upper yield point followed by a lower yield point and a plateau. Corresponding to the Lüders plateau, a plastic front formed at the clamped end of the sample and traveled along its length. Thus, heterogeneity of plastic straining clearly stemmed from the boundary conditions. Strain hardening started when the plastic front reached the opposite end, and was eventually accompanied by PLC bands. Again, the bands started at the clamped end and propagated continuously along the sample. Their bandwidth could show oscillations, tightly associated with small serrations occurring in the stress vs. strain curve (although small serrations also occur independently of bandwidth oscillations). Due to the fine resolution length scale, details of the three-dimensional stress field in the band area could be observed, as Fig.23 shows. Behind the trailing edge of the band, the tensile stress was found to be larger on the upper

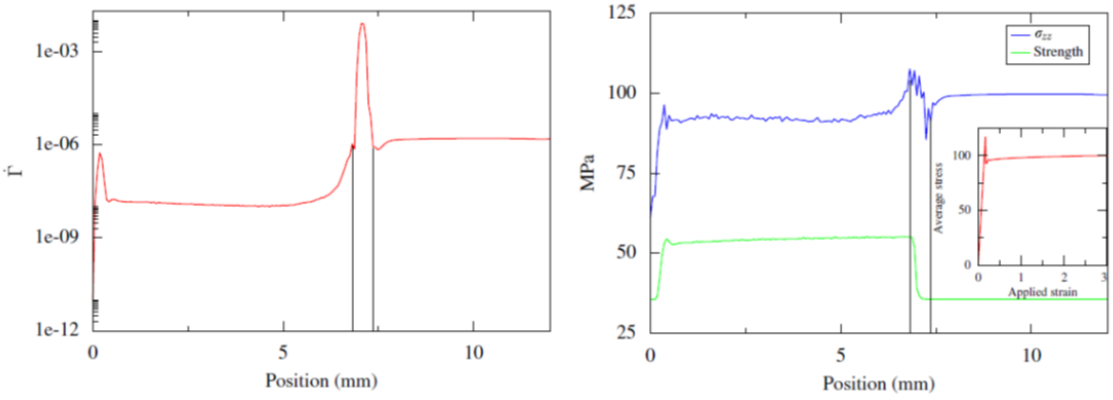

Figure 23: Structure of a Lüders band in simulated tensile test of $Al-Mg$ single crystal. Applied strain rate $\dot{\epsilon}_a = 5 \times 10^{-5} s^{-1}$. Data along axial z-axis on sample mid-plane at 1.9% strain; left: equivalent strain rate in s^{-1}, right: axial normal stress σ_{zz} and material strength $(\tau_a + \tau_h + \tau_{sp})$. The inset shows the corresponding part of the stress-strain curve. Note that the normal stress at the head of the plastic front corresponds to the stress at the upper yield-point. After [41], with permission of the Editor.

face than on the lower face of the sample, indicating the presence of a bending moment. Material strength defined by the sum $(\tau_a + \tau_h + \tau_{sp})$ appearing in Eq.22, and shown in Fig.23, was also larger in this area, due to increased levels of strain hardening and solute pinning stress generated by the band. Large excess dislocation density regions were found along the leading edge of the bands separating the highly strained bands from their lowly strained surroundings ahead. These dislocations induce large incompatibility stresses reflected in the high level of normal stress seen in Fig.23 in this area, as well as a prevailing role of these stresses in band propagation. The implication of excess dislocations in band propagation was further assessed by turning off the evolution of their density in Eq.16, which unambiguously stopped band propagation. However, the prediction of a continuous band propagation is at odds with the experimentally observed hopping propagation of the bands in this range of applied strain rates. The origin of such a discrepancy could reside either in an overvalued plastic relaxation time $\tau_R = \tau_0/\mu \sum_s \rho_m b v_s$ or in an excess of incompatibility stresses. Further investigations will be needed to fully resolve this issue in future work.

Like all other time series encountered in this paper, the stress time series obtained during the period of stress serrations were pre-processed to remove long term trends from work hardening, then unfolded as an orbit into the reconstructed phase space. The orbit was plotted by first performing a singular value decomposition of the trajectory matrix. The principal values decreased rapidly, with the third one being only 5% of the first and largest one. The restriction of the orbit to the subspace spanned by the eigenvectors corresponding to the three largest principal values revealed a compact attractor, of which the correlation dimension was computed using the Grassberger-Procaccia algorithm. The value $\nu \approx 2.9$ was obtained, which may be compared with $\nu \approx 2.7$ for the experiments conducted on $Cu - 10\% Mg$ single crystals in [55]. However, due to the limited number of data, the scaling range was only an order of magnitude, as compared to two orders of magnitude for the experimental time series. The Lyapunov spectrum of exponents was also calculated, using the modified Eckmann's algorithm. A positive Lyapunov exponent was found, along with other characteristics of a chaotic, dissipative system: the presence of a near-zero exponent and a negative sum of exponents. From the Lyapunov spectrum, the Lyapunov dimension was determined to be $D_{KY} \approx 2.85$, in line with the correlation

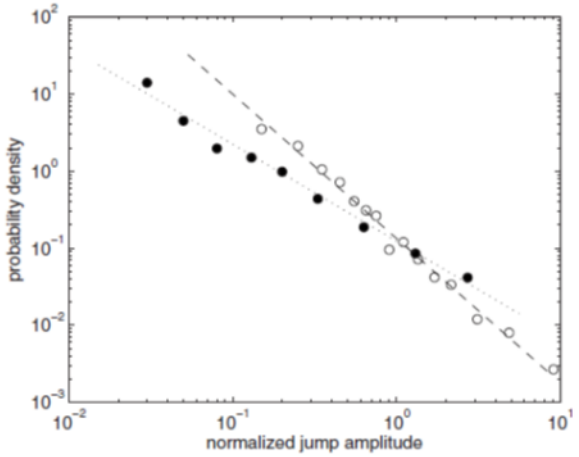

Figure 24: Probability density of event size in numerical simulation of flat Cu whisker in tension at strain rate $\dot{\epsilon}_a = 10^{-3}s^{-1}$. The event size is defined either as a stress drop size (filled circles; the dotted trend line shows an $\alpha_s = 1.2$ slope) or the size of a stress rate burst (open circles; the dashed trend line shows an $\alpha = 1.9$ slope). After [42], with permission of the Editor.

dimension. Clearly, all the evidence from these different methods converged and pointed to a chaotic structure similar to that found in the experiments on $Cu - 10\%Mg$ single crystals [55].

- Single crystal without Dynamic Strain Aging In reference [42], simulations of the tensile test at strain rate $\dot{\epsilon}_a = 10^{-3}s^{-1}$ of a flat pure Cu whisker of dimensions $200\,\mu m \times 30\,\mu m \times 2400\,\mu m$ were carried out. The sample was clamped to the left end, while the right end was submitted to constant velocity. The finite element mesh contained 27648 brick elements in a $24 \times 6 \times 192$ arrangement. The elastic response was taken to be anisotropic with elastic constants C_{11}, C_{12}, and C_{44}. In the response of the sample, elastic loading was followed by the Lüders phenomenon: a yield drop associated with plastic activity localized near the clamped end, followed by a plateau. Again, heterogeneity of plastic straining stemmed from boundary conditions. Along the plateau, the plastic activity spread over the sample through the motion of a plastic front, before strain hardening took place. The hardening trend was quasi-linear over a short period of time, along which bursts in stress rate were observed, but with a much smaller size than in the presence of DSA. The statistical analysis of the stress time series showed power-law scaling in stress rate burst size distribution, with exponent $\alpha = 1.9 \pm 0.1$, and in stress drop size distribution, with exponent $\alpha_s = 1.2 \pm 0.1$, without inconsistency as shown in [42] (see Fig.24). The predicted scaling exponent for stress drop size distribution was consistent with the experimental value $\alpha \approx 1.1$ reported in [55] for $Cu - 10\%Al$ single crystals, where the addition of solute elements also induced plastic events with a much larger stress drop size.

  In view of these results, various two-dimensional simulations (far more tractable than three dimensional ones) were carried out in order to check for possible variations in the scaling exponent. The influence of various factors on the strain rate time series obtained at a material point in the sample, such as numerical parameters (mesh size, time step), sample size and shape, boundary conditions and material behavior, was systematically analyzed. For example, the mesh size was refined by a factor 2, the time step divided by a factor 10, the applied strain rate $\dot{\epsilon}_a$ reduced by a factor 10, the sample size varied by a factor 10. Yet, the power law with exponent $\alpha \approx 2$ was invariably found for the event size probability density distribution. Using a slender sample did not have effects either. Possible

influence of the material behavior was also investigated by simulating the plasticity of ice single crystals, keeping the geometry and loading conditions unchanged. Indeed, Cu and ice have very different crystalline structures and material behavior. The latter switches from thermally activated in Cu to viscous drag in ice, with a small SRS parameter $n = 2$ and virtually no strain hardening (τ_h kept small and constant) in Eq.25. Nevertheless, the probability density for event size showed again scaling distributions with exponent $\alpha \approx 2$, a value in line with the experimental data obtained from the high-resolution DIC experiments on Cu single crystals carried out in [42], already alluded to in Sections 4.4.2,5.2.1 but not reported here, and with AE experimental data in ice single crystals [50, 51].

5.2.3 Discussion

From the results of the single crystal simulations reported above, the chaotic behavior demonstrated at medium strain rates in the presence of DSA [41] and the scaling behavior of the plastic activity shown in the absence of DSA [42] both imply that spatial coupling in single crystals derives from the long-range stresses arising from the presence of dislocations and from the short range interactions encountered in dislocation transport through the material. These conclusions can be drawn at the scale of the sample from its stress vs. time response, as well as at slip plane level from the strain-rate field. At sample scale, the scaling behavior of the small size plastic bursts was shown to be robust, with an apparently universal scaling exponent value $\alpha \approx 2$ in the event size distribution. At slip plane level, the large size plastic bursts occurring in the presence of DSA were shown to obey instead a chaotic dynamics.

The chaotic behavior demonstrated by single crystals is similar to that observed in polycrystals, although spatial coupling is presumably weaker in the former, but the numbers are different: the correlation dimension and Lyapunov dimension are smaller in single crystals, implying that fewer independent variables are needed to account for their dynamics. However, our initial questions as to whether the coupling mechanisms suggested for single crystals could generate the sequence of plastic localization patterns and dynamics observed as the applied strain rate spans the negative SRS range remain partially unanswered. Further, unexpected questions arose from our results: the sheer contrast between the statistics of small scale events in uniform plastic flow and that of the large scale events observed in jerky flow in the presence of DSA, most prominently at low/medium strain rates where Gaussian behavior of large scale events is observed, raises again the issues encountered when monitoring simultaneously AE emission and macroscopic stress drops in polycrystals, and still pending in single crystals, namely: in a single experiment, does the observed dynamical regime depend on the resolution length scale of the observations? Are the plastic events observed at micro and macroscale built from the same basic mechanisms? In particular, do the microscale plastic events contribute to the macroscale ones, and if they do, in which manner? Additional multiscale experiments conducted in single crystals of a solute alloy, as well as additional single crystal simulations involving parametric studies, would perhaps allow to further ascertain the conjectures of Sections 4.

6 Overall discussion

Because it features remarkable self-organized patterns at macroscopic scale, the PLC effect has set off an enormous amount of investigations, among which, however, few paid attention to the plastic events concurrently occurring on a smaller scale. In the mean time, the AE associated with the small scale plastic events occurring during smooth uniform plastic flow have been independently detected and their self-organization described [50, 51]. The statistical and multifractal data obtained from $Al - 3\%Mg$ polycrystals in [18, 66] suggest that this relative independence of the descriptions of stable and jerky flow was actually inappropriate, because the underlying plasticity processes revealed in both by AE at mesoscopic scale are similar. Three

major results of these joint serrations-AE studies plead for such a conjecture:

- Multifractality is observed in the time series of AE events size unresolved in mechanical testing, either during the initial smooth plastic flow occurring before the critical strain ϵ_{cr} for the onset of serrations, or the jerky flow occurring after ϵ_{cr}.

- The scaling ranges found for the distributions of AE event size observed during serrated flow overlap their counterparts for the corresponding stress–time series, and extend further to time scales shorter by an order of magnitude. Hence, the multifractal character of the AE distributions is not a by-product of the multifractality of the stress drops distributions. Instead, it provides fresh evidence for a similar nature of the dislocation processes, should they belong to plastic events of mesoscopic or macroscopic size.

- Nevertheless, the differences in the scaling exponents of the macroscopic and mesoscopic event size distributions confirm, if needed, that differences do exist in the nature of the dynamic regimes at work at the different resolution length scales. Such differences were anyway clear when comparing the stress drop and AE events size distributions, particularly at low and medium strain rates, where peaked distributions of stress drop size were observed, while AE events sizes were characterized by scale-free statistics. From this comparison, it is clear that chaos characterized at macroscopic scale does not translate into chaos at the level of individual dislocations [97].

Clues allowing to explain the contrast between the mesoscale and macroscale event size distributions were found in the series of amplitudes and durations of AE events shown in Fig.12. Indeed, the AE amplitude recorded at the instants of macroscopic stress drops remains of the order of the amplitudes accompanying smooth plastic flow, whereas strong bursts concurrently occur in the series of AE event durations. The insensitivity of the amplitude of AE activity to the occurrence of stress drops, which is instead invariably signaled by bursts in its duration, suggest that PLC bands do not occur by the motion of larger-than-usual dislocation subsets, but by the synchronization, triggered by elastic waves, of usual glide events.

As indicated in Sections 5.1.2 and 5.1.3, the synchronization conjecture complements and substantiates the interpretation laid out to explain the sequence of peaked to power-law statistics of stress drops, namely that spatial coupling decreases with the ratio t_R/t_L, where t_R is the plastic relaxation time and t_L the reloading time between stress drops. According to this interpretation, very little time is allowed at high strain rates for the plastic relaxation of internal stresses during the reloading time intervals t_L because $t_R/t_L \gg 1$. Therefore, a high degree of spatial correlation exists between events. In addition and independently, the critical threshold for dislocation unpinning of the N-shaped characteristic flow stress vs. strain rate curve shown in Fig.17, is relatively low and displays a small downward convexity at high applied strain rates [22], which drives all dislocation subsets close to the critical threshold for instability as stress increases. As a result, dislocation glide events of any size triggered by elastic waves (although in a limited range of relatively small events, due to the low critical threshold level) can occur at any time. Scale-free distributions of plastic event size are therefore induced in that range in both the AE and stress drop time series. In such conditions, the synchronization of plastic events only plays a minor role, and the sample is "close" to accommodating the applied loading through a spatially uniform plastic strain rate field.

As the applied strain rate $\dot{\epsilon}_a$ is decreased to small strain rates, the reloading time becomes much larger than the plastic relaxation time ($t_R/t_L \ll 1$), which allows almost complete plastic relaxation of internal stresses. Therefore, spatial correlations become much weaker and the correlation distance much shorter than at high strain rates. In addition, the critical threshold for dislocation unpinning is now much larger, because the obstacles to dislocation motion are much stronger. Hence the stress serrations are much larger than at high strain rates. Further,

the characteristic flow stress vs. strain rate curve now shows a sharp downward convexity at this point. Hence the threshold stress is reached nearly simultaneously in various parts of the sample. As a result, the nucleation of plastic events occurs at any point, which implies less correlation with the previous PLC band. The system becomes overdriven, as a large fraction of the dislocations remain strongly pinned on their obstacles. The accommodation of the applied strain rate $\dot{\epsilon}_a$ is therefore achieved through large localized plastic strain rate offsets from the threshold of instability (see Fig.22). According to the AE statistical and multifractal analyses, these large events are due to the synchronization of standard-size plastic events at mesoscale, and not to the unpinning of very large dislocation subsets. Hence, the synchronized plastic events are more localized in space and time, with a quasi-Gaussian macroscopic size distributions. As discussed above in Section 5.1.3, the large plastic events obtained through synchronization of regular scale events form static bands randomly distributed, while the distribution of the small plastic events detected through their associated AE is still controlled by the remaining spatial correlations, as testified by their scale-free character.

At medium strain rates, when the plastic relaxation time is of the order of the reloading time ($t_R \approx t_L$), an intermediate situation is found between the previous two cases. Comparing to high strain rates, the internal stresses are partially relaxed. Spatial correlation is weaker, but still existing, and the correlation distance shorter. Further, the critical threshold for dislocation unpinning is larger, since the obstacles to dislocation motion are stronger. As a result, the stress serrations are medium-sized compared to their counterparts at small and high strain rates, with irregular bell-shaped size distributions. As discussed in Section 5.1.3, these macroscopic plastic events are associated with hopping bands and chaotic dynamics, while the mesoscopic event size distributions still retain scale free character.

7 Conclusions

The jerky flow of dilute alloys in a tensile test offers the fascinating example of an easily controllable system where such complex dynamical regimes as chaos and SOC can both be observed at the expense of a simple adjustment of the driving strain rate $\dot{\epsilon}_a$. Such a wealth of dynamic behavior results from the various combinations provided by the non linear local behavior deriving from DSA and the non local spatial coupling due to both long range incompatibility stresses and short range interactions encountered by dislocations during their transport through the material. Perhaps even more amazing, both chaos and SOC can be observed concurrently in a single test, by changing the resolution length scale of the observations. Chaos is characterized only at the macroscopic scale of the stress serrations, and only in specific conditions, namely at intermediate applied strain rates $\dot{\epsilon}_a$, for which spatial coupling is marginal and obstacles to dislocation motion relatively strong. SOC is more pervasive. Its scale invariance can be characterized at the macroscopic scale of stress serrations at strain rates sufficiently high to ensure strong spatial coupling and weak obstacles to dislocation motion, and also at all applied strain rates at the mesoscopic scale of the AE associated with small scale plastic events, or even at both scales in a single experiment. In short, SOC is the rule, and chaos the exception. Actually, the increased strength of obstacles offered by DSA at low and medium strain rates is needed for the occurrence of the peaked event size distributions associated with chaos [97]. Strong obstacles shift the dislocation ensembles away from the critical threshold for unpinning, and their dynamics from criticality. This feature is demonstrated by Fig.22, which shows that most dislocations are close to the critical threshold in the scaling regime, whereas a large fraction of them remains in the pinned state, far from criticality, in the chaotic regime, and even more so in the quasi-random regime at low applied strain rates. Further, the multiscale experiments showed in polycrystals, through concurrent AE and stress time series monitoring, that, in the presence of strong obstacles at low and medium applied strain rates, collective unpinning of dislocations occurs more by the synchronization of regular size plastic events than by outsized

events, whereas this plastic events synchronization process is relatively ineffective in the presence of weak obstacles. To wrap up all these arguments, it might be stated that medium strain rates provide adequate conditions for the occurrence of chaos, from the triple point of view of the plastic events size, their synchronization and their spatial coupling, whereas high strain rates lead to sufficiently weak obstacles and sufficiently strong spatial coupling to establish SOC among macroscale events, these conditions being satisfied at all strain rates for mesoscale events.

Acknowledgements

The authors are deeply indebted to Ladislas P. Kubin for leading them towards a better understanding of dislocation dynamics, by his encyclopedic knowledge of dislocation processes and the acuity of his scientific judgment, as well as for his faithful friendship and fidelity. Much of this work could not have been accomplished without G. Ananthakrishna, A.J. Beaudoin, Y. Bréchet and Y. Estrin. CF particularly wishes to thank G. Ananthakrishna, CNRS, IFCPAR and JNCASR, for numerous stays in the company of Ladislas at the Indian Institute of Science in Bangalore, as they have been highlights of this research. The participation to this work of numerous colleagues and students of the Indian Institute of Science, the University of Illinois at Urbana-Champaign and the University of Lorraine is deeply acknowledged, among them: M.S. Bharathi, Y. Bougherira, D. Entemeyer, S. Kok, S. Noronha, L. Quaouire, I.V. Shashkov, V. Taupin and S. Varadhan, for their dedicated involvement.

References

[1] Portevin A and Le Chatelier F 1923 Sur un phénomène observé lors de l'essai de traction d'alliages en cours de transformation *C.R. Acad. Sci.* Paris **176** 507-510

[2] Rodrigues P 1984 Serrated plastic flow *Bull. Mat. Sci.* **6** 653–663

[3] Yilmaz A 2011 The Portevin - Le Chatelier effect: A review of experimental findings *Sci. Tech. Adv. Mat.* **12** (6) 1-16

[4] Tamimi S, Andrade-Campos A and Pinho-da-Cruz J 2015 Modelling the Portevin-Le Chatelier effects in aluminium alloys: a review *J. Mech. Behav. Mater.* **24**(3-4) 67–78

[5] Cottrell A H 1953, *Dislocations and Plastic Flow in Crystals* Oxford: University Press

[6] Friedel J 1964 *Dislocations* Oxford: Pergamon Press

[7] Li M and Lege DJ 1998 Serrated flow and surface markings in aluminum alloys *J. Eng. Mat. Tech.* Transactions of the ASME **120** (1) 48–56

[8] Cieslar M, Fressengeas C, Karimi A and Martin JL 2003 Portevin–Le Chatelier effect in biaxially strained Al–Fe–Si foils *Scripta Mater.* **48** 1105–1110

[9] Kang J, Wilkinson D, Jain M, Embury J, Beaudoin A, Kim S, Mishira R and Sachdev A 2006 On the sequence of inhomogeneous deformation processes occurring during tensile deformation of stripcast AA 5754 *Acta Mater.* **5** 4(1) 209–218

[10] Delafosse D, Lapasset G and Kubin L 1993 Dynamic strain ageing and crack propagation in the 2091 Al–Li alloy *Scripta Metall. Mater.* **29** (11) 1379–1384

[11] Fournier L, Delafosse D and Magnin T 2001 Oxydation induced intergranular cracking and Portevin–Le Chatelier effect in nickel base superalloy 718 *Mat. Sci. Eng. A* **316** (1–2) 166–173

[12] Mach J, Kang J, Beaudoin A and Wilkinson D 2006 Heterogeneity in plastic deformation *Mat. Sci. Forum* **519–521** 85–92

[13] Garat V, Cloué JM, Poquillon D and Andrieu E 2008 Influence of Portevin–Le Chatelier effect on rupture mode of alloy 718 specimens *J. Nuclear Mat.* **375** (1) 95–101

[14] McCormick PG 1972 A model for the Portevin-Le Chatelier effect in substitutional alloys *Acta Metall.* **20** 351–354

[15] van den Beukel A 1975 Theory of the effect of dynamic strain ageing on mechanical properties *Phys. Status Solidi (a)* **30** 197-206

[16] Penning P 1972 Mathematics of the Portevin-Le Chatelier effect 1972 *Acta metall.* **20** 1169-1175

[17] Louat N 1981 On the theory of the Portevin-Le Chatelier effect *Scripta metall.* **15** 1167-1170

[18] Lebyodkin MA, Kobelev NP, Bougherira Y, Entemeyer D, Fressengeas C, Gornakov VS, Lebedkina TA and Shashkov IV, 2012 On the similarity of plastic flow processes during smooth and jerky flow: statistical analysis *Acta Mater.* **60** 3729–3740

[19] Brindley BJ and Worthington PJ 1970 Yield-point phenomena in substitutional alloys *Metall. Rev.* **15** 1 101-114

[20] Pink E and Grinberg A 1981 Serrated flow in a ferritic stainless steel *Mater. Sci. Eng.* **51** 1-8

[21] Chihab K, Estrin Y, Kubin LP and Vergnol J 1987 The kinetics of the Portevin-Le Chatelier bands in an $Al-5at\%Mg$ alloy *Scripta Metall.* **21** 203-208

[22] Kubin LP, Fressengeas C and Ananthakrishna G, 2002 Collective behavior of dislocations in plasticity, In: Nabarro FRN, Hirth JP, editors *Dislocations in solids*, vol. 11. North-Holland Publishing Company, Amsterdam, 101-192

[23] Ryu WH, Ko WS, Isano H, Yamada R, Ahn H, Yoo GH, Yoon KN, Park ES, Saida J 2023 Sustainable steady-state serrated flow induced by modulating deformation sequence in bulk metallic glass *J. Alloys Compd.* **2023** 946, 169308

[24] Han Z, Ding C, Liu G, Yang J, Du Y, Wei R, Chen Y, Zhang G Analysis of deformation behavior of VCoNi medium-entropy alloy at temperatures ranging from 77 K to 573 K *Intermetallics* **2021** 132, 107126

[25] Brechtl J, Chen S, Lee C, Shi Y, Feng R, Xie X, Hamblin D, Coleman AM, Straka B, Shortt H et al 2020 A Review of the Serrated-Flow Phenomenon and Its Role in the Deformation Behavior of High-Entropy Alloys *Metals* 10, 1101

[26] Lebyodkin M, Brechtl J, Lebedkina T, Wen K, Liaw PK, Shen T 2023 Scaling and Complexity of Stress Fluctuations Associated with Smooth and Jerky Flow in FeCoNiTiAl High-Entropy Alloy, *Metals* 13, 1770

[27] Yin S, Wang Z, Brechtl J, Zhang H, Zhang M, HanJ, Wang Z, Qiao J 2024 Shear band velocity and activation volume during shear deformation by acoustic emission in a Zr-based bulk metallic glass *J. Non-Crystalline Sol.* **625** 122767

[28] Hao R, Liu G, Wang Z, Yang H, Liaw PK, Qiao J 2023 A prediction model for the failure threshold in a CoNiV medium-entropy alloy *J. Appl. Phys.* **134** 135101

[29] Bergé P, Pomeau Y and Vidal C 1984 *Order within chaos, towards a deterministic approach to turbulence* New York: Wiley

[30] Ananthakrishna G and Valsakumar MC 1983 Chaotic flow in a model for repeated yielding *Physics Letters A*, **95** (2) 69-71

[31] Strogatz SH 2000 From Kuramoto to Crawford: Exploring the Onset of Synchronization in Populations of Coupled Oscillators *Physica D: Nonlinear Phenomena* **143** 1-20

[32] Bak P, Tang C, Wiesenfeld K 1987 Self-organized criticality: An explanation of the 1/f noise *Phys. Rev. Lett.* **59** 381

[33] Jensen HJ 1998 *Self-Organized Criticality* Cambridge University Press

[34] Halsey TC, Jensen MH, Kadanoff LP, Procaccia I and Shraiman BI 1986 Fractal measures and their singularities: The characterization of strange sets *Phys. Rev. A* **33**, 1141; Erratum 1986 *Phys. Rev. A* **34**, 1601

[35] Kubin LP and Estrin Y 1985 The Portevin-Le Chatelier effect in deformation with constant stress rate *Acta Metall.* **3** 397-407

[36] Kubin LP and Estrin Y 1990 Evolution of dislocation densities and the critical conditions for the Portevin-Le Chatelier effect, *Acta Metall. Mater.* **38** (5) 697-708

[37] Fressengeas C, Beaudoin AJ, Lebyodkin M, Kubin LP and Estrin Y 2005 Dynamic strain aging: A coupled dislocation—solute dynamic model. *Mat. Sci. Eng. A* **400–401** 226–230

[38] Lebyodkin M, Bréchet Y, Estrin Y and Kubin LP 1995 Statistics of the catastrophic slip events in the Portevin-Le Chatelier effect, *Phys. Rev. Lett.* **74** 4758-4761

[39] Lebyodkin M, Dunin-Barkowskii L, Bréchet Y, Estrin Y and Kubin LP 2000 Spatio-temporal dynamics of the Portevin-Le Chatelier effect: experiment and modelling *Acta Mater.* **48** 2529-2541

[40] Kok S, Bharathi MS, Beaudoin AJ, Fressengeas C, Ananthakrishna G, Kubin LP and Lebyodkin M 2003 Spatial coupling in jerky flow using polycrystal plasticity *Acta Mater.* **51** 3651–3662

[41] Varadhan S, Beaudoin AJ and Fressengeas C, 2009 Lattice incompatibility and strain-aging in single crystals *J. Mech. Phys. Solids* **57** 1733–1748

[42] Fressengeas C, Beaudoin AJ, Entemeyer D, Lebedkin T, Lebyodkin M and Taupin V 2009 Dislocation transport and intermittency in the plasticity of crystalline solids *Phys. Rev. B* **79** 014108

[43] Lebyodkin M, Bougherira Y, Lebedkina T and Entemeyer D 2020 Scaling in the Local Strain-Rate Field during Jerky Flow in an $Al-3\%Mg$ Alloy *Metals* **10** 134

[44] Brechtl J, Feng R, Liaw PK, Beausir B, Lebedkina T and Lebyodkin M 2023, Mesoscopic-scale complexity in macroscopically-uniform plastic flow of an $Al_{0.3}CoCrFeNi$ high-entropy alloy, *Acta Mater.* **242**, 118445

[45] Lebyodkin MA and Lebedkina TA, 2006 Multifractal analysis of evolving noise associated with unstable plastic flow, *Phys. Rev. E* **73** 036114

[46] Mathis K and Chmelik F 2012 Exploring Plastic Deformation of Metallic Materials by the Acoustic Emission Technique, in: Sikorsky W (Ed.), *Acoustic Emission*, InTech, Rijeka, Croatia, 23–48

[47] Vinogradov A, Iasnikov IS and Merson DL 2019 Phenomenological approach towards modelling the acoustic emission due to plastic deformation in metals *Scripta Mater.* **170** 172-176

[48] Lebyodkin MA, Shashkov IV, Lebedkina TA, Mathis K, Dobroň P and Chmelik F 2013 Role of superposition of dislocation avalanches on the statistics of acoustic emission during plastic deformation *Phys. Rev. E* **88** 042402.

[49] Lebyodkin MA, Shashkov IV, Lebedkina TA and Gornakov VS 2017 Experimental investigation of the effect of thresholding on temporal statistics of avalanches *Phys. Rev. E* **95** 032910

[50] Weiss J, Ben Rhouma W, Richeton T, Dechanel S, Louchet F and Truskinovsky L, From Mild to Wild Fluctuations in Crystal Plasticity 2015 *Phys. Rev. Lett.* **114** 105504

[51] Weiss J, Grasso JR 1997 Acoustic emission in single crystals of ice *J. Phys. Chem. B* 101:6113

[52] Noronha SJ, Ananthakrishna G, Quaouire L, Fressengeas C and Kubin LP 1997 Chaos in the Portevin - Le Chatelier effect, *Int. J. Bifurcation Chaos* **7**:2577

[53] Takens F Detecting Strange Attractors in Fluid Turbulence 1981 in Rand DA and Young LS eds. *Symposium on Dynamical Systems and Turbulence* Springer Lecture Notes in Mathematics **898** 366-381

[54] Ananthakrishna G, Fressengeas C, Grosbras M, Vergnol J, Engelke C, Plessing J, Neuhauser H, Bouchaud E, Planès J and Kubin LP 1995 On the existence of chaos in jerky flow *Scripta Metall. Mater.* **32** 1731

[55] Ananthakrishna A, Noronha SJ, Fressengeas C and Kubin LP 1999 Crossover from chaotic to Self-Organized Critical - type of dynamics in the jerky flow of single crystals *Phys. Rev. E* **60**: 5455

[56] Broomhead DS and King GP 1986 Extracting qualitative dynamics from experimental data *Physica D* **20** 217–236

[57] Eckmann JP, Kamphorst SO, Ruelle D and Ciliberto S 1986 Liapunov exponents from time series *Phys. Rev. A* **34** 4971-4979

[58] Frederickson P, Kaplan JL, Yorke ED and Yorke JA 1983 The Liapunov dimension of strange attractors *J. Diff. Eq.* **49** 185-207

[59] Mandelbrot BB 1983 *The Fractal Geometry of Nature* Henry Holt and Company, New York, NY, USA

[60] Grassberger P and Procaccia I 1983 Measuring the strangeness of strange attractors *Physica* 9D 189-208

[61] Chhabra AB and Jensen RV 1989 Direct determination of the $f(\alpha)$ singularity spectrum *Phys. Rev. Lett.* **62**, 1327

[62] Bharathi MS, Lebyodkin L, Ananthakrishna G, Fressengeas C and Kubin LP 2001 Multifractal burst in the spatiotemporal dynamics of jerky flow *Phys. Rev. Lett.* **87**:165508

[63] Bharathi MS, Lebyodkin L, Ananthakrishna G, Fressengeas C and Kubin LP 2002 The hidden order behind jerky flow, *Acta Mater.* **50** 2813–2824

[64] Weiss J, Grasso JR, Miguel MC, Vespignani A and Zapperi S 2001 Complexity in dislocation dynamics: model. *Mater. Sci. Eng. A* 309:360

[65] Richeton T, Weiss J, Louchet F, Dobroň P and Chmelik F 2007 Critical character of plasticity from AE experiments in hcp and fcc metals *Kovove Mater.* **45**:149

[66] Lebyodkin MA, Kobelev NP, Bougherira Y, Entemeyer D, Fressengeas C, Lebedkina TA and Shashkov IV, 2012 On the similarity of plastic flow processes during smooth and jerky flow in dilute alloys, *Acta Mater.* **60** 844-850

[67] Lebyodkin M, Bréchet Y, Estrin Y and Kubin LP 1996 Statistical behaviour and strain localization patterns in the Portevin-Le Chatelier effect *Acta Mater.* **44**, 11, 4531-4541

[68] Venkadesan S, Murthy KPN, Rajasekhar S and Valsakumar MC 1996 Evidence for chaos in an experimental time series from serrated plastic flow *Phys. Rev. E* **56**:611

[69] Thevenet D, Mliha-Touati M and Zeghloul A 1999 The effect of precipitation on the Portevin-Le Chatelier effect in an $Al-Zn-Mg-Cu$ alloy, *Mater. Sci. Eng. A* **266** 175–182

[70] Kobelev P, Lebyodkin MA and Lebedkina TA 2017 Role of self-organization of dislocations in the onset and kinetics of the macroscopic plastic instability, *Metall. Mater. Trans. A* **48** 965-974

[71] Lebedkina TA, Zhemchuzhnikova DA and Lebyodkin MA 2018 Correlation versus randomization of jerky flow in an $Al-Mg-Sc-Zr$ alloy using acoustic emission, *Phys. Rev. E* **97** 013001

[72] Lebedkina TA, Bougherira Y, Entemeyer D, Lebyodkin MA and Shashkov IV 2018 Crossover in the scale-free statistics of acoustic emission associated with the Portevin-Le Chatelier instability *Scripta Mater.* **148** 47-50

[73] Devincre B, Hoc T and Kubin LP 2008 Dislocation mean free paths and strain hardening of crystals *Science* **320** 1745

[74] Vinogradov A, Merson DL, Patlan V and Hashimoto S 2003 Effect of solid solution hardening and stacking fault energy on plastic flow and acoustic emission in $Cu-Ge$ alloys, *Mater. Sci. Eng.* A **341**, 57-73

[75] Richeton T, Dobroň P, Chmelík F, Weiss J and Louchet F 2006 On the Critical Character of Plasticity in Metallic Single Crystals, *Mater. Sci. Eng.* A **424** 190

[76] Král R, Dobroň P, Chmelík F, Koula V, Rydlo M and Janeček M 2007 A qualitatively new approach to acoustic emission measurements and its application to pure aluminium and $Mg-Al$ alloys, *Kovove Mater.* **45** 159–163

[77] Agletdinov E, Drozdenko D, Harcuba P, Dobroň P, Merson D and Vinogradov A 2020 On the long-term correlations in the twinning and dislocation slip dynamics, *Mat. Sci. Engng.* A. **777** 139091

[78] Lebyodkin MA, Lebedkina TA, Chmelík F, Lamark TT, Estrin Y, Fressengeas C and Weiss J 2009 Intrinsic structure of acoustic emission events during jerky flow in an Al alloy, *Phys. Rev.* B **79**, 174114

[79] Feder J 2013 *Fractals*, Springer, Berlin/Heidelberg, Germany

[80] Shibkov AA, Gasanov MF, Zheltov MA, Zolotov AE and Ivolgin VI 2016 Intermittent plasticity associated with the spatio-temporal dynamics of deformation bands during creep tests in an $Al-Mg$ polycrystal, *Int. J. Plast.* **86** 37

[81] Shashkov IV, Lebyodkin MA and Lebedkina TA 2012 Multiscale study of acoustic emission during smooth and jerky flow in an $AlMg$ alloy, *Acta Mater.* **60** 6842–6850

[82] Lebyodkin MA, Shashkov IV, Lebedkina TA and Gornakov VS 2014 Multiscale analysis of acoustic emission during plastic flow of Al and Mg alloys: from microseconds to minutes, *Mater. Sci. Forum* **783-786** 204-209

[83] Shashkov IV 2012 Multiscale study of the intermittency of plastic deformation by acoustic emission method, PhD thesis, University of Lorraine

[84] Tan PN, Steinbach M, Karpatne A, Kumar V 2019 *Introduction to Data Mining* (Pearson, New York, second edition)

[85] Allen RV 1982 Automatic phase pickers, their present use and future prospects *Bull. Seismol. Soc. Am.* **72** 6, 225-242

[86] Wang Z 2009 Detection of weak earthquake signals based on wavelet analysis *Prog. Explor. Geophys.* **32** 3, 182-185

[87] Canel V 2020 Acoustic monitoring of damage in cemented granular materials: experiments and simulations, PhD thesis, University Grenoble Alpes

[88] Lebyodkin M, Dunin-Barkovskii L, Bréchet Y, Kubin L and Estrin Y 1997, Kinetics and statistics of jerky flow: experiments and computer simulations, *Mater. Sci. Eng.* A **234-236** 115-118

[89] Burridge R and Knopoff L 1967 Model and theoretical seismicity, *Bull. Seismol. Soc. Am.* **57** 341-371

[90] Carlson JM and Langer JS 1989 Mechanical model of an earthquake fault, *Phys. Rev.* A **40** 6470-6484

[91] Cartwright JHE, Eguíluz VM, Hernández-García E and Piro O 1999 Dynamics of Elastic Excitable Media, *Int. J. Bifurcation and Chaos* **9** 2197-2202

[92] Hadamard J 1903 *Leçons sur la propagation des ondes et les équations de l'hydrodynamique* Paris: Herman

[93] Ait-Amokhtar H, Fressengeas C and Bouabdallah K 2015 On the effects of the Mg content on the critical strain for the jerky flow of $Al-Mg$ alloys *Mat. Sci. Engng. A* **631** 209-213

[94] Acharya A 2001 A model of crystal plasticity based on the theory of continuously distributed dislocations. *J. Mech. Phys. Solids* **49** 761–784

[95] Acharya A 2003 Driving forces and boundary conditions in continuum dislocation mechanics *Proc. Roy. Soc. A* **459** 1343–1363

[96] Acharya A and Roy A 2006 Size effects and idealized dislocation microstructure at small scales: predictions of a phenomenological model of mesoscopic field dislocation mechanics: part I. *J. Mech. Phys. Solids* **54** 1687–1710

[97] Ananthakrishna G and Fressengeas C 2005 Comment on: Dislocation dynamics is chaotic, *Scripta Mater.* **52** 425–428